Geophysical Journal International

Geophys. J. Int. (2021) **225,** 789–810
Advance Access publication 2021 January 12
GJI Seismology

doi: 10.1093/gji/ggab005

PRISM3D: a 3-D reference seismic model for Iberia and adjacent areas

P. Arroucau [1,2,3] S. Custódio,[2] C. Civiero,[2,3] G. Silveira,[2,4] N. Dias,[2,4] J. Díaz,[5] A. Villaseñor[6] and T. Bodin [7]

[1] *Electricité de France (EDF), DIPNN-DI-TEGG,* 905 *Avenue du Camp de Menthe,* 13097 *Aix-en-Provence, France. E-mail: pierre.arroucau@edf.fr*
[2] *Instituto Dom Luiz (IDL), Faculdade de Ciências, Universidade de Lisboa, Campo Grande,* 1749-016 *Lisboa, Portugal*
[3] *Dublin Institute for Advanced Studies (DIAS), Geophysics Section,* 5 *Merrion Square, Dublin* D02 Y006, *Ireland*
[4] *Instituto Superior de Engenharia de Lisboa, Instituto Politécnico de Lisboa,* 1959-007 *Lisboa, Portugal*
[5] *Institute of Earth Sciences Jaume Almera, Consejo Superior de Investigaciones Científicas (ICTJA-CSIC), Barcelona, Spain*
[6] *Institute of Marine Sciences, Consejo Superior de Investigaciones Científicas (ICM-CSIC), Barcelona, Spain*
[7] *Université de Lyon, ENS Lyon, CNRS, UMR* 5276 *LGL-TPE, F-*69622 *Villeurbanne, France*

Accepted 2020 December 29. Received 2020 December 19; in original form 2020 March 23

SUMMARY

We present PRISM3D, a 3-D reference seismic model of *P*- and *S*-wave velocities for Iberia and adjacent areas. PRISM3D results from the combination of the most up-to-date earth models available for the region. It extends horizontally from 15°W to 5°E in longitude, 34°N to 46°N in latitude and vertically from 3.5 km above to 200 km below sea level, and is modelled on a regular grid with 10 and 0.5 km of grid node spacing in the horizontal and vertical directions, respectively. It was designed using models inferred from local and teleseismic body-wave tomography, earthquake and ambient noise surface wave tomography, receiver function analysis and active source experiments. It includes two interfaces, namely the topography/bathymetry and the Mohorovičić (Moho) discontinuity. The Moho was modelled from previously published receiver function analysis and deep seismic sounding results. To that end we used a probabilistic surface reconstruction algorithm that allowed to extract the mean of the Moho depth surface along with its associated standard deviation, which provides a depth uncertainty estimate. The Moho depth model is in good agreement with previously published models, although it presents slightly sharper gardients in orogenic areas such as the Pyrenees or the Betic-Rif system. Crustal and mantle *P*- and *S*-wave wave speed grids were built separately on each side of the Moho depth surface by weighted average of existing models, thus allowing to realistically render the speed gradients across that interface. The associated weighted standard deviation was also calculated, which provides an uncertainty estimation on the average wave speed values at any point of the grid. At shallow depths (<10 km), low *P* and *S* wave speeds and high V_P/V_S are observed in offshore basins, while the Iberian Massif, which covers a large part of western Iberia, appears characterized by a rather flat Moho, higher than average V_P and V_S and low V_P/V_S. Conversely, the Betic-Rif system seems to be associated with low V_P and V_S, combined with high V_P/V_S in comparison to the rest of the study area. The most prominent feature of the mantle is the well known high wave speed anomaly related to the Alboran slab imaged in various mantle tomography studies. The consistency of PRISM3D with previous work is verified by comparing it with two recent studies, with which it shows a good general agreement.The impact of the new 3-D model is illustrated through a simple synthetic experiment, which shows that the lateral variations of the wave speed can produce traveltime differences ranging from –1.5 and 1.5 s for *P* waves and from –2.5 and 2.5 s for *S* waves at local to regional distances. Such values are far larger than phase picking uncertainties and would likely affect earthquake hypocentral parameter estimations. The new 3-D model thus provides a basis for regional studies including earthquake source studies, Earth structure investigations and geodynamic modelling of Iberia and its surroundings.

Key words: Composition and structure of the continental crust; Composition and structure of the mantle; Structure of the Earth; Body waves; Seismicity and tectonics; Surface waves and free oscillations.

1 INTRODUCTION

3-D seismic wave speed models are of primary importance for earthquake source, Earth structure and geodynamics investigations. For instance, 3-D earth models can be used to improve the accuracy of earthquake location (e.g. Chen *et al.* 2006; Wagner *et al.* 2013) or moment tensor inversion (e.g. Hingee *et al.* 2011), the results of which are key for understanding seismotectonics and assessing earthquake hazard. Earthquake hypocentral parameters are classically determined assuming 1-D, radially symmetric seismic wave speed models (e.g. Lienert *et al.* 1986), thus relying on the implicit assumption that lateral topography and wave speed variations may safely be neglected. However, several studies have shown that the use of 3-D earth models has the potential to improve the accuracy of earthquake parameters, particularly in regions where the Earth displays strong lateral heterogeneities (e.g. Husen *et al.* 2003; Hingee *et al.* 2011; Wagner *et al.* 2013; Béthoux *et al.* 2016). In Earth structure studies, high-resolution 3-D seismic models are useful starting models. In teleseismic body-wave tomography, for instance, accurate 3-D starting models help minimize the contributions to the traveltime anomalies from unresolved crustal structure and, when using data from transportable arrays, allow to capture long wavelength features in the mantle that would otherwise be unresolved (e.g. Rawlinson *et al.* 2016). When combined with other observations, 3-D seismic velocity models allow to interpret and discuss geodynamic processes, particularly in complex regions of the Earth (e.g. Stefano *et al.* 1999; Smith *et al.* 2009; Wang *et al.* 2013).

In this paper, we focus on the region encompassing Iberia, northwest Africa and the adjacent offshore areas, namely the Atlantic and Western Mediterranean domains (Fig. 1). The study area runs from the Betic-Rif system in the South to the Pyrenees range in the North. It is located on the northeast Atlantic margin, along the plate boundary that separates Nubia, to the South, from Eurasia, to the North. It lies between the Gloria fault, to the West, a major oceanic strike-slip fault that acts as plate boundary (Lynnes & Ruff 1985; DeMets *et al.* 2010; Batista *et al.* 2017; Omira *et al.* 2019), and the Mediterranean domain, to the East, where plate convergence is accommodated by a complex tectonic regime (Faccenna *et al.* 2014, and references therein). This compressive regime led to the accretion of Iberia to Europe, uplift of the Pyrenees orogen and inversion of Mesozoic rifts (Rosenbaum *et al.* 2002; de Vicente & Vegas 2009). As in Iberia, the intracontinental Atlas Mountains in Morocco were also uplifted during the Cenozoic by inversion of Triassic–Jurassic transtensional troughs (e.g. Zeyen *et al.* 2005; de Lamotte *et al.* 2009). In southern Spain and northern Morocco, plate compression and roll-back of the Mediterranean oceanic slab resulted in the uplift of the Betics and Rif, respectively (e.g. Royden 1993). Although the region is located within an overall convergent domain, parts of it have undergone extension in the Miocene, when the convergence velocity between Africa and Eurasia decreased and slab retreat initiated throughout the Mediterranean realm (Royden 1993; Wortel & Spakman 2000; Faccenna *et al.* 2004). In the Valencia Trough, which corresponds to the westward continuation of the Provençal basin, extension occurred between ∼26 and ∼16 Ma, followed by the clockwise rotation of the Balearic Islands (Vergés & Sàbat 1999). Further South, the Alboran extensional basin, together with the Betic-Rif orogen, form the Gibraltar Arc System. This system, which started to form ∼30 Ma, is one of the most complex arc–backarc domains in our planet in terms of geodynamic evolution (Gutscher *et al.* 2002). Multiple models have been proposed to explain its present-day configuration. Currently, the most consensual model involves the interaction of southern Iberia and northwestern Africa with a narrow, westward retreating slab, a process which appears to be slowing down (Gutscher *et al.* 2012; Serpelloni *et al.* 2013; Civiero *et al.* 2020). The complex geological history of our study region, which involved active geodynamic processes such as successive orogenic and rifting episodes (Pinheiro *et al.* 1996; Zitellini *et al.* 2004; Duarte *et al.* 2011), results in substantial spatial variations in topography, crustal thickness and lithologies (Díaz *et al.* 1993; Simancas *et al.* 2003; Fernàndez *et al.* 2004).

In spite of the current low tectonic convergence rate, the study area exhibits remarkable levels of seismic activity, both onshore and offshore. Current studies, based on data recorded both on land and on the seafloor, indicate that earthquakes occur either in thickened, normal or thinned continental crust, as well as in the oceanic crust and lithospheric uppermost mantle (Custódio *et al.* 2015; Grevemeyer *et al.* 2015, 2016, 2017; Veludo *et al.* 2017; Silva *et al.* 2017). A reliable 3-D *P*- and *S*-wave speed model of both the crust and upper mantle is therefore needed for accurate seismic wave propagation and geodynamic modelling.

Iberia, northwest Africa and the adjacent offshore areas have been exceptionally well-covered by seismic instrumentation in recent years. Over 50 permanent broadband seismometers currently operate in the region, including networks PM (Instituto Português do Mar e da Atmosfera, I.P. 2006), ES (Instituto Geografico Nacional, Spain 1999), GE (GEOFON Data Centre 1993), IP, LX (Instituto Dom Luiz (IDL)-Faculdade De Ciências Da Universidade De Lisboa 2003), SS, WM [San Fernando Royal Naval Observatory (ROA) 1996], CA (Institut Cartogràfic I Geològic De Catalunya 1984), IU (Albuquerque Seismological Laboratory ASL 1988) and MN (MedNet Project Partner Institutions 1988). In addition, temporary deployments, including IberArray (Institute Earth Sciences 'Jaume Almera' CSIC (ICTJA Spain) 2007; Díaz *et al.* 2010), WILAS (Dias *et al.* 2010; Custódio *et al.* 2014), PICASSO (Levander & Humphreys 2009; Palomeras *et al.* 2014) and Nearest (Geissler *et al.* 2010), have densely covered the region in the past decade, both onshore and offshore. Active seismic experiments have also been undertaken with the goal of characterizing the Earth's inner structure beneath Iberia (Díaz *et al.* 1993, 2010, 2016; Afilhado *et al.* 2008; Sallarès *et al.* 2011; Martínez-Loriente *et al.* 2014, and references therein). A number of models for the Earth's structure have been derived from these rich seismic data sets for the Rif (Gil *et al.* 2014), the Atlas (Ayarza *et al.* 2014), the Cantabrian Mountains (Pulgar *et al.* 1996; Pedreira *et al.* 2015), Variscan Iberia (Flecha *et al.* 2009; Ehsan *et al.* 2015), the Iberian Rift System (Seillé *et al.* 2015) as well as Central Iberia (Andrs *et al.* 2019). However, a single model that covers the entire region and has a good description of Moho topography, as well as of *P* and *S* wave speeds, in the crust and in the mantle, is still missing. In this paper, we merge the most up-to-date seismic models

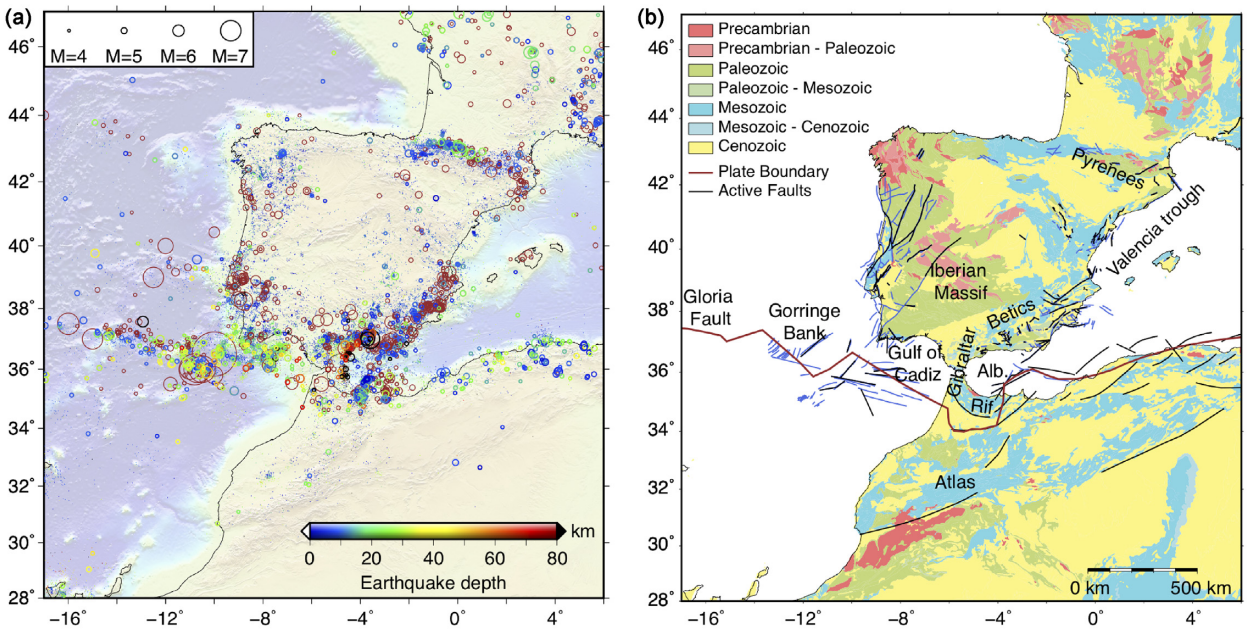

Figure 1. Maps of Iberia (SW Europe) and northwest Africa, showing: (a) Earthquake epicentres (circles) overlaid on topography and bathymetry (SRTM30+, Becker *et al.* 2009). The parameters of $M > 4$ earthquakes are taken from the SHARE database up to 2006 (Grünthal *et al.* 2013; Stucchi *et al.* 2013) and complemented with those from the compilation of Custódio *et al.* (2016) from 2007 to 2016. The magnitudes of these earthquakes are shown by the size of the circles. High-quality instrumental epicentres of smaller magnitude ($M < 4$) earthquakes that occurred between 1996 and 2016 are displayed as dots (Custódio *et al.* 2016). Epicentres are colour-coded according to earthquake depth, with a colourscale saturated at a depth of 80 km. Earthquakes with undetermined depths are plotted in brown. (b) Simplified geological units of Iberia, NW Africa and SW France (USGS *et al.* 1997a,b). Also displayed are the Eurasia–Africa Plate boundary (brown, Bird 2003), potentially active faults documented in the SHARE database (black, Basili *et al.* 2013; Vilanova *et al.* 2014) and high-resolution fault traces (including probable and debated faults, blue, Zitellini *et al.* 2009; Cabral 2012; García-Mayordomo *et al.* 2012). Labelled regions: Gorringe bank, Iberian massif, Gulf of Cadiz, Gibraltar strait, Atlas mountains, Rif, Alboran sea (Alb.), Betics, Valencia trough and Pyrenees.

available for the study area in order to build a unified 3-D reference earth model for Iberia, northern Africa and adjacent offshore areas, which we name PRISM3D. PRISM3D contains a 3-D description of *P*- and *S*-wave velocities, from the surface down to 200 km. In addition, PRISM3D explicitly describes the crust–mantle boundary (Moho) as a surface of laterally varying depth. PRISM3D is made openly available through the IRIS earth Model Collaboration platform (https://ds.iris.edu/ds/products/emc/).

2 MODEL INPUTS

We used the most recent models of Earth structure available for the study region as inputs to PRISM3D. The crust–mantle interface (Moho) was designed based on EPcrust (Molinari & Morelli 2011) and further modified using results from dedicated studies. EPcrust is an integrated crustal model for Europe that describes three crustal layers: sediments, upper crust and lower crust. The model portrays the topography of the surface, Moho and layer interfaces, as well as lateral variations of *P*- and *S*-wave velocities within each layer. Model parameters are reported on latitude–longitude grids of 0.5° × 0.5°, down to the crust–mantle boundary. We started from the EPcrust Moho and modified it using: (1) Moho depth values from Deep Seismic Sounding (DSS) compilations (Chevrot *et al.* 2014; Díaz & Gallart 2009; Diaz *et al.* 2016) as well as single experiment refraction lines (Afilhado *et al.* 2008; Sallarès *et al.* 2011; Martínez-Loriente *et al.* 2014) from which we digitized additional, individual Moho depth profiles and (2) receiver function analyses (Salah 2014; Chevrot *et al.* 2015; Mancilla & Diaz 2015; Dündar *et al.* 2016). Fig. 2 shows the individual Moho depth values for all models, along with their spatial distribution.

Reference crustal *P* and *S* wave speeds were taken from EPcrust and subsequently combined with models inferred from: (1) ambient noise and teleseismic surface wave tomography (Macquet *et al.* 2014; Pasyanos *et al.* 2014; Gaudot 2016; Palomeras *et al.* 2017; Silveira *et al.* 2016), (2) local earthquake tomography (Lbadaoui *et al.* 2012; El Moudnib *et al.* 2015; Veludo *et al.* 2017), (3) active seismic experiments (Afilhado *et al.* 2008; Sallarès *et al.* 2011; Martínez-Loriente *et al.* 2014) and (4) geological modelling (Theunissen *et al.* 2017, who shared their *a priori* tomographic model based on geology).

Mantle V_P and V_S were obtained from: (1) P_n and S_n tomography (Díaz *et al.* 2013), (2) teleseismic *P*-wave traveltime tomography (Amaru 2007; Monna *et al.* 2013; Bezada *et al.* 2014; Bonnin *et al.* 2014; Chevrot *et al.* 2014; Pasyanos *et al.* 2014; Villaseñor *et al.* 2015) and (3) surface wave tomography (Schivardi & Morelli 2011; Pasyanos *et al.* 2014; Palomeras *et al.* 2017).

Tables 1 and 2, as well as Figs 2 and 3, show the characteristics and areal coverage of the input models.

3 METHOD

The region is modelled as a grid extending horizontally from 15°W to 5°E in longitude, from 34°N to 46°N in latitude, and vertically from 3.5 km above to 200 km below sea level. Grid node spacing is 0.5 km in the vertical direction, and ∼10 km in longitude and latitude.

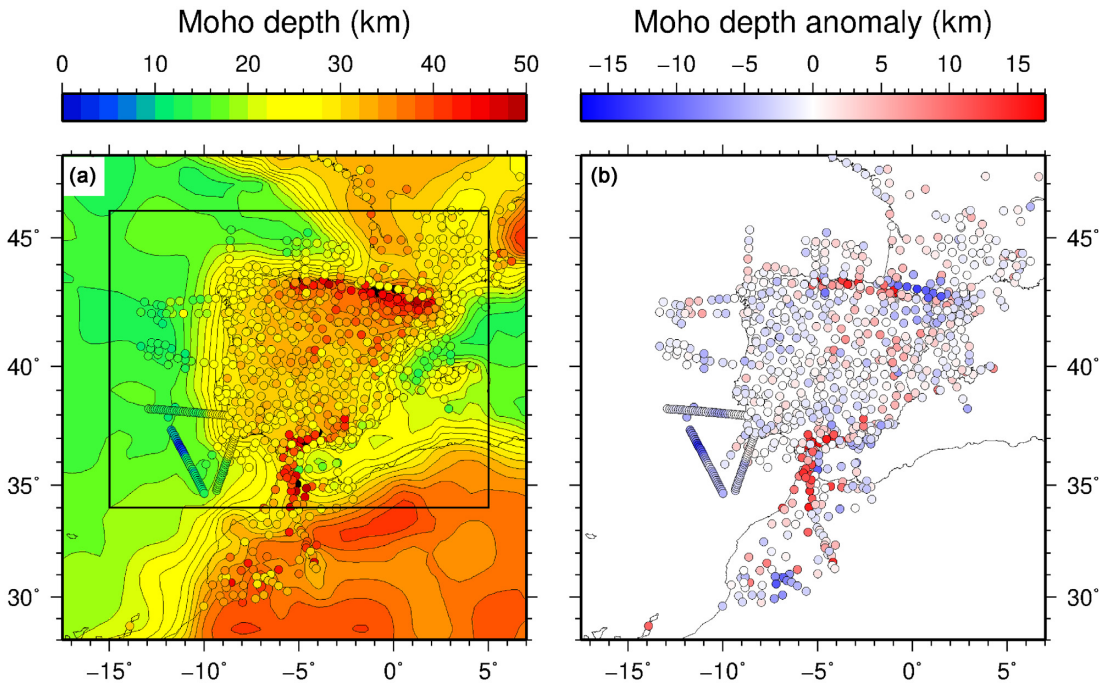

Figure 2. Input Moho depth values compiled from previous active source and receiver function studies (see text and Table 1 for details and references). (a) Coloured circles show absolute Moho depth values with respect to sea level (positive downwards). The EPcrust Moho depth model is plotted in the background (Molinari & Morelli 2011). The black rectangle depicts the limits of our study area. (b) Moho depth anomalies calculated as the difference between the absolute values reported in the compiled studies and the reference Moho depth of EPcrust.

Table 1. Input models for the crust–mantle boundary (Moho).

Reference	Type of study
Molinari & Morelli (2011)	Integration of previous models
Díaz & Gallart (2009); Diaz *et al.* (2016)	Integration of deep seismic soundings
Salah *et al.* (2011)	Receiver functions
Chevrot *et al.* (2015)	Receiver functions
Mancilla & Diaz (2015)	Receiver functions
Dündar *et al.* (2016)	Receiver functions
Afilhado *et al.* (2008)	Deep seismic sounding
Sallarès *et al.* (2011)	Deep seismic sounding
Martínez-Loriente *et al.* (2014)	Deep seismic sounding

3.1 Model interfaces

We started by setting the surface topography and seafloor bathymetry to that of ETOPO1 (Amante & Eakins 2009). In order to avoid aliasing, we applied a Gaussian lowpass filter with 10 km standard deviation. Next, we used the probabilistic surface reconstruction technique introduced by Bodin *et al.* (2012) in order to integrate the Moho depth estimates from the studies listed in Table 1. The method is based on the reversible jump Markov chain Monte Carlo algorithm (rj-McMC, Green 1995). It consists of a Bayesian inference approach aimed at combining information known *a priori* with that from observed input data. The result is an ensemble of surfaces, from which the *a posteriori* probability distribution of the surface lateral depth variations can be estimated.

We first expressed observed Moho depth values as anomalies with respect to the Moho depth reference surface of EPcrust (Molinari & Morelli 2011) by simple subtraction. Fig. 2 shows the reference surface and input Moho depth values that were used in this work (Fig. 2a) and the corresponding Moho depth anomalies (Fig. 2b) that were subsequently interpolated. The advantage of considering depth anomalies rather than absolute depths is that the Moho depth surface is only updated where the data requires it, while remaining equal to the reference where no data is available or where data noise is too high.

The Moho depth surface was discretized using Voronoi cells, whose number and location were not fixed but rather were allowed to vary in the course of the procedure. Here, we considered an *a priori* uniformly distributed number of cells ranging from 3 to 200. The *a priori* depth anomaly was set to 0 km for the entire region (corresponding to the EPcrust model), and its uncertainty was modelled as a uniform distribution ranging from –30 to +30 km. By using such a wide range we imposed nearly no constraints on the solution in order to make the most of the information provided by the input data. In the rj-McMC algorithm, the level of required data fit and relative weighting between different data types are determined by the data, in combination with *a priori* information. Thus, they do not need to be set to fixed, subjective values. For each data set, we used this ability to determine the value of a multiplicative, dimensionless constant to apply to data uncertainties provided by model authors, with an *a priori* uniform distribution ranging from 0.05 to 10, so as to impose as little *a priori* constraints as possible on the solution.

Table 2. Input models for V_P and V_S structure.

Reference	Type of study	Depth (km)	Weight (P/S)
	Crust		
Molinari & Morelli (2011)	Compilation of previous studies (V_P, V_S)	0–Moho	0.1 / 0.1
Macquet *et al.* (2014)	Ambient noise tomography (V_S)	0–60	0.25 / 0.75
Gaudot (2016)	Ambient noise tomography (V_S)	0–100	0.25 / 0.75
Silveira *et al.* (2016)	Ambient noise tomography (V_S)	0–50	0.125 / 0.5
Palomeras *et al.* (2017)	Surface wave tomography (V_S)	0–250	0.25 / 0.75
Lbadaoui *et al.* (2012)	Local earthquake tomography (V_P, V_S)	0–50	1.0 / 1.0
El Moudnib *et al.* (2015)	Local earthquake tomography (V_P)	0–100	1.0 / 0.125
Veludo *et al.* (2017)	Local earthquake tomography (V_P, V_S)	0–35	1.0 / 1.0
Afilhado *et al.* (2008)	Deep seismic sounding (V_P)	0–25	1.0 / 0.5
Sallarès *et al.* (2011)	Deep seismic sounding (V_P)	0–25	1.0 / 0.5
Martínez-Loriente *et al.* (2014)	Deep seismic sounding (V_P)	0–25	1.0 / 0.5
Pasyanos *et al.* (2014)	Surface wave traveltime tomography (V_P, V_S)	0–400	0.05 / 0.05
Bezada *et al.* (2014)	Teleseismic P-wave traveltime tomography (V_P)	0–700	0.125 / 0.05
Bonnin *et al.* (2014)	Teleseismic P-wave traveltime tomography (V_P)	0–700	0.125 / 0.05
Theunissen *et al.* (2017)	Geological model (V_P, V_S)	0–60	0.5 / 0.5
	Mantle		
Díaz *et al.* (2013)	P_n and S_n wave tomography (V_P, V_S)	sub-Moho	1.0 / 1.0
Pasyanos *et al.* (2014)	Surface wave traveltime tomography (V_P, V_S)	0–400	0.1 / 0.1
Palomeras *et al.* (2017)	Surface wave tomography (V_S)	0–250	0.25 / 1.0
Chevrot *et al.* (2014)	Teleseismic P-wave traveltime tomography (V_P)	0–500	1.0 / 0.25
Monna *et al.* (2013)	Teleseismic P-wave traveltime tomography (V_P)	0–600	1.0 / 0.25
Bezada *et al.* (2014)	Teleseismic P-wave traveltime tomography (V_P)	0–700	1.0 / 0.25
Bonnin *et al.* (2014)	Teleseismic P-wave traveltime tomography (V_P)	0–700	1.0 / 0.25
Villaseñor *et al.* (2015)	Teleseismic P-wave traveltime tomography (V_P)	0–700	1.0 / 0.25
Amaru (2007)	Teleseismic P-wave traveltime tomography (V_P)	5–2815	1.0 / 0.25
Schivardi & Morelli (2011)	Teleseismic surface wave traveltime tomography (V_S)	70–490	0.25 / 1.0

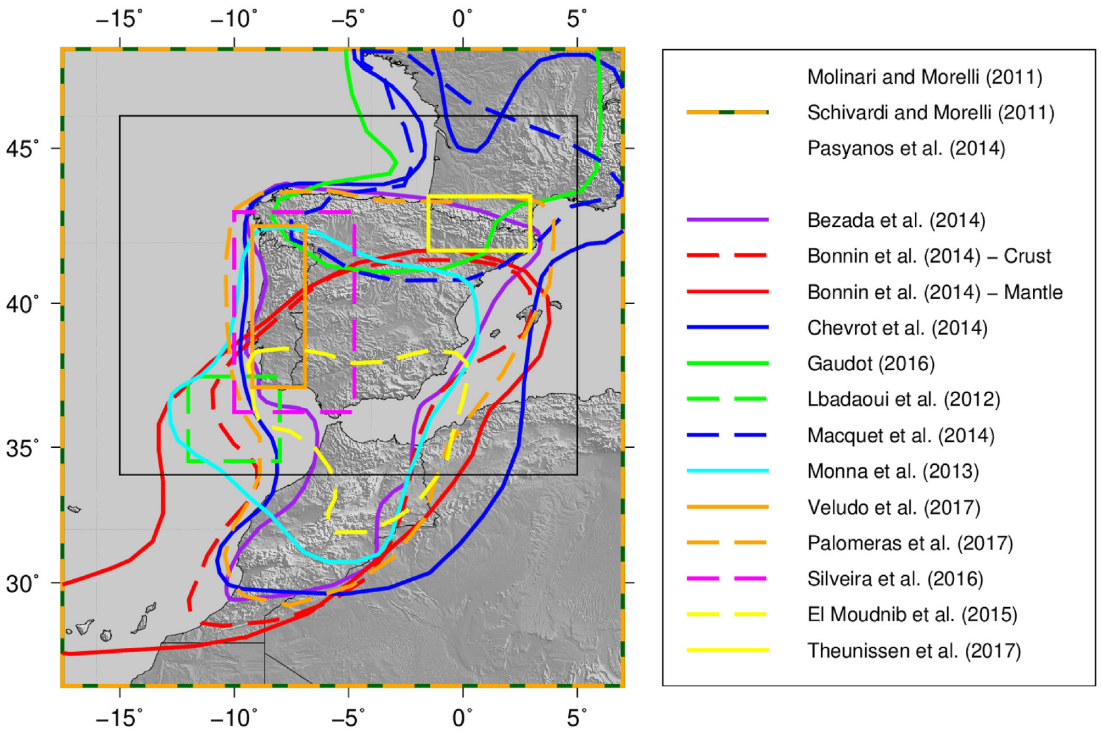

Figure 3. Areas covered by each of the input V_P and V_S models considered in this work. The black rectangle depicts the limits of our study area (Table 2).

The full ensemble solution consisted of 50 000 000 Moho depth anomaly models, which were converted to Moho depth models by adding them back to the initial reference surface. Meaningful statistical information associated with the *a posteriori* probability function can be extracted from the ensemble. Fig. 4(a) shows the mean Moho depth, which was obtained by averaging a subset of uncorrelated Voronoi models from the ensemble solution. Fig. 4(b) shows the corresponding standard deviation, which can be interpreted as the vertical error of the inferred Moho depth surface.

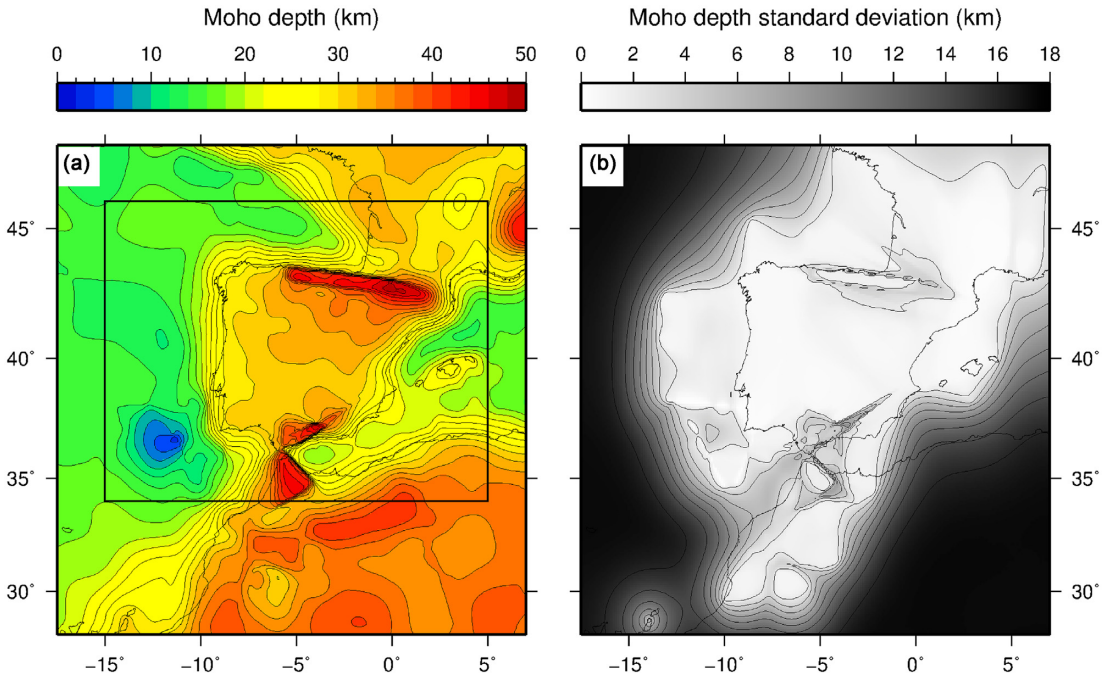

Figure 4. (a) Final Moho depth model, obtained by interpolating receiver functions and deep seismic sounding results using the rj-McMC algorithm (average of ensemble solutions). The black rectangle shows the limit of our study area. (b) Moho depth error (standard deviation of ensemble solutions). Moho depth error is quite low over most of Iberia (<500 m), increasing up to values of 2–4 km in the northern coast of Spain and in the Gibraltar region, where the Moho displays sharp gradients. Moho depth in North Africa is only well constrained in NW Morocco, as a result of good data coverage in the region.

In this work we choose to consider the mean (and associated standard deviation) as an estimator of the full posterior distribution. Another choice could have been made, such as the median or the mode, which would have produced different results, hence a different final model. This emphasizes the inherent difficulty to infer one single model from the ensemble, as discussed in (Bodin *et al.* 2012).

3.2 Crustal structure

After having defined the topography of the Earth's surface and of the Moho interface, we adopted a 'shrink-and-stretch' strategy to modify the crustal part of EPcrust. As stated in the previous section, EPcrust consists of three layers (sediments, upper crust and lower crust), each of which is characterized by laterally varying thickness and P and S wave speeds. Sediment thickness was left unchanged because the models that we used did not provide additional information that would have justified the modification of that parameter, which already results from a compilation of existing models (Molinari & Morelli 2011). Upper and lower crust were modified using the ratio between PRISM3D and EPcrust crustal thicknesses (without sediments). Thus, the initial relative thickness of upper and lower crust layers was preserved.

The final V_P and V_S crustal grids were subsequently computed as the weighted average of the modified EPcrust model and of the other models listed in the upper part of Table 2. The models considered include results from geological modelling (Theunissen *et al.* 2017), ambient noise and teleseismic surface wave tomography (Macquet *et al.* 2014; Pasyanos *et al.* 2014; Gaudot 2016; Palomeras *et al.* 2017; Silveira *et al.* 2016), local earthquake tomography (Lbadaoui *et al.* 2012; El Moudnib *et al.* 2015; Veludo *et al.* 2017), active seismic studies (Afilhado *et al.* 2008; Sallarès *et al.* 2011; Martínez-Loriente *et al.* 2014), and teleseismic tomography (Bezada *et al.* 2013; Bonnin *et al.* 2014). Tomographic depth slices from the different models were first resampled to PRISM3D's horizontal grid node spacing using the nearest neighbor algorithm of GMT (Wessel & Smith 1998). Then, depth slices were computed every 0.5 km by linear interpolation. Note that since the grid node spacing of the input models is in all cases larger than that of PRISM3D, no anti-alias filtering was needed prior to that stage.

Validity limits provided by the authors were used to define polygons enclosing regions of full weight for each model (Fig. 3), with a weight of 1.0 inside the polygon and 0.0 outside. In order to prevent edge effects, those full weight regions were smoothed out by means of a Gaussian lowpass filter with 50 km standard deviation. Weights denote the level of confidence assigned to each model. Although quantitative by nature, they result essentially from a qualitative ranking of the models based on the methodology and type of data they were obtained from, allowing to implicitly account for the differences in resolution of the different models. In the crust, active source studies provide the most accurate models and were therefore assigned the highest weights, with a value of 1.0. So were local earthquake tomography models, which are primarily sensitive to crustal structure. Lower weights, ranging between 0.5 and 0.75, were assigned to results from ambient noise surface wave studies, which are sensitive to the crustal structure but produce smooth models and do not allow to image sharp velocity contrasts. Finally, even lower weights of ∼0.05–0.1 were assigned to teleseismic tomography results, whose sensitivity to crustal structure is low. When only either V_P or V_S was available, the second velocity was calculated from the V_P/V_S ratio. For the crust, V_P/V_S was determined from receiver function results, interpolated using the same procedure as that used for Moho depth surface reconstruction. These indirect wave speed values were assigned lower weights than the original ones (Table 2). Profile models from active seismic source studies that could be obtained were also incorporated in PRISM3D. In order to assimilate these 2-D profiles into our 3-D model, we extended

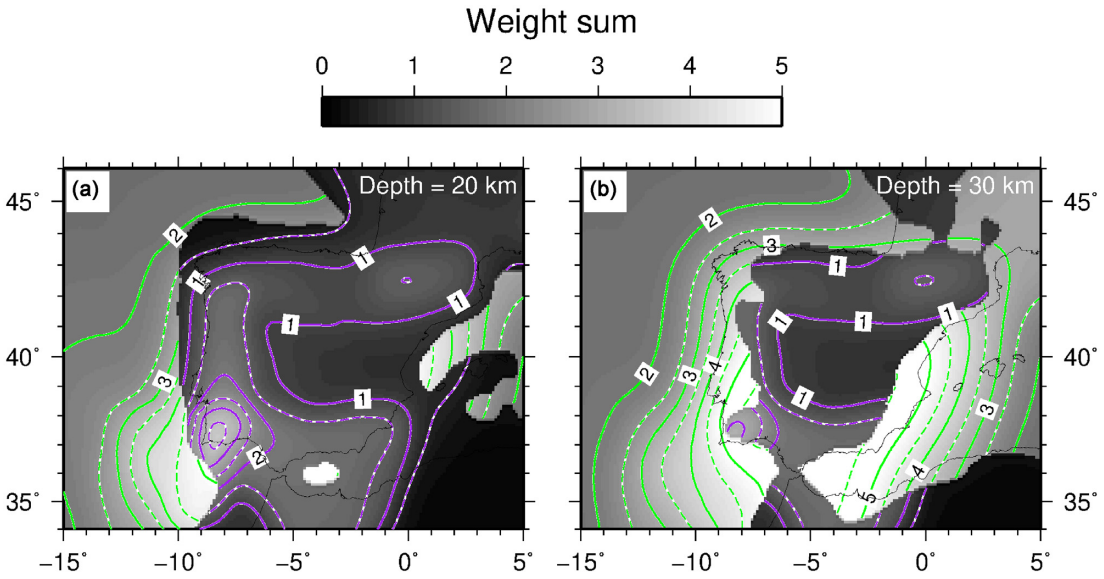

Figure 5. Weight sum maps at: (a) 20 km and (b) 30 km depth. Contour lines are shown in purple for the crust and in green for the mantle. Following Molinari & Morelli (2011), we consider weight sum as a proxy for information content and use that quantity to delineate the confidence region where our model can be considered better constrained. In order to account for the better coverage of mantle models but finer resolution of crustal models, a distinct threshold is chosen for each. We propose an arbitrary limit of 0.5 for the crust and 2.0 for the mantle as defining the confidence region of PRISM3D. E-supplement movies Mov1 and Mov2 show the variation of weight sums, for the *P*- and *S*-wave velocity models, respectively, from the surface down to 200 km depth.

the profiles laterally, with a weight decreasing exponentially with increasing distance from the profile. V_P and V_S were bounded to maximum values of 7.5 and 4.2 km s^{-1}, respectively, in order to prevent mantle wave speeds to bias our crustal model. Finally, a weight function decreasing exponentially with depth was also applied to models obtained by ambient noise tomography, local earthquake tomography and seismic profiles, in order to account for their decaying resolution at depth. As a result, the EPcrust reference model has a relatively higher weight in the lower crust. Note that although it was possible to use information from a large number of DSS profiles previously collected by different authors for Moho depth surface modelling, only a few refraction profiles could on the other hand be obtained and included in the velocity grid of PRISM3D. More models from active source experiments will be incorporated in future versions of the models. The integration of models such as those used in the recently published work of (Lozano *et al.* 2020), for instance, could greatly enhance the quality of PRISM3D.

3.3 Mantle structure

In order to model mantle structure, we started by setting sub-Moho *P*- and *S*-wave speeds to the P_n and S_n tomographic values of Díaz *et al.* (2013), so that the first grid node below the Moho was assigned the corresponding value from the P_n and S_n tomographic model. Then, mantle wave speeds below 60 km depth were computed from the weighted average of the 3-D *P*- and *S*-wave tomographic models listed in the lower part of Table 2. These include teleseismic *P*-wave traveltime tomography models (Monna *et al.* 2013; Bezada *et al.* 2014; Bonnin *et al.* 2014; Chevrot *et al.* 2014; Villaseñor *et al.* 2015; Amaru 2007) and *S*-wave models obtained from teleseimic surface wave data inversion (Schivardi & Morelli 2011; Pasyanos *et al.* 2014; Palomeras *et al.* 2017). The global model Litho1.0 of Pasyanos *et al.* (2014), obtained from the inversion of Rayleigh and Love wave dispersion curves, was also included despite its coarseness, because it provides a full coverage of the region for both *P*- and *S*-wave speeds. Similar to what was done for the crust, whenever only V_P or V_S was available, the other quantity was calculated from the V_P/V_S ratio, which in the case of the mantle was simply taken from AK135 (Kennett *et al.* 1995).

In the case of the mantle, all models were considered equally good and assigned a weight of 1.0. Lower weights were assigned to either V_P or V_S if that quantity was calculated from V_P/V_S. Note that since the crust and mantle were modelled separately, their weights do not commensurate with each other. Thus, while the weights are useful to identify better resolved regions within the crust, or alternatively within the mantle, they cannot be used to compare the resolution of the crust with that of the mantle. Similar to crustal modelling, mantle horizontal wave speed slices were re-sampled and interpolated in depth every 0.5 km. Then, wave speeds between the Moho and a depth of 60 km were obtained from the weighted average of V_P and V_S directly below the Moho (Díaz *et al.* 2013) and the model V_P and V_S at 60 km, with an exponentially decreasing depth-dependent weight applied to the values from Díaz *et al.* (2013). This approach resulted in a weight of 1.0 for the P_n and S_n tomographic values of Díaz *et al.* (2013) at Moho depth, and of ∼0.007 at 60 km depth.

3.4 Confidence region and uncertainty estimation

PRISM3D integrates models with varying areal coverage (Fig. 3) and information content. As a result, our region of interest is not evenly covered and wave speed values in different regions are not equally well constrained. In order to define a confidence region and discriminate areas that are well covered from areas that are not, we adopted the strategy of Molinari & Morelli (2011) and used the sum of the weights as a proxy for information content. This strategy allows the identification of zones that are better covered and hence potentially better resolved than others. These are the regions for which more models and/or higher weights were used. This approach is also similar, to some extent, to the vote map strategy of Hosseini *et al.* (2018) or Shephard *et al.* (2017). Fig. 5 shows the

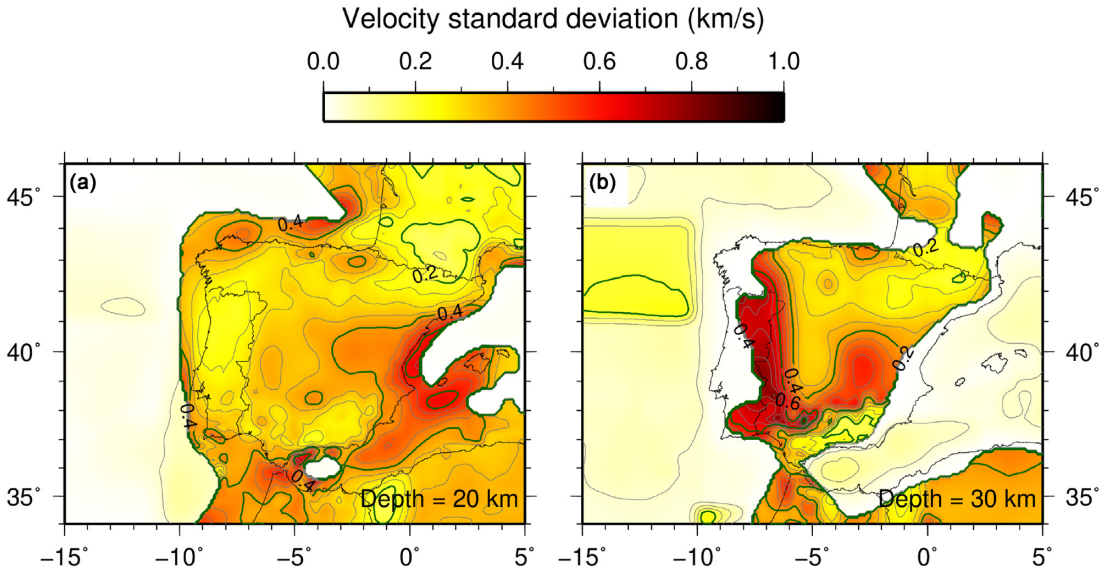

Figure 6. Weighted standard deviation maps at: (a) 20 km and (b) 30 km depth. The weighted standard deviation represents the velocity variability among the models used as input to build PRISM3D. Thin grey contour lines are drawn every 0.05 km s^{-1}, while the thick dark green contour lines are drawn in steps of 0.2 km s^{-1}. E-supplement movies Mov3 and Mov4 show the variation of weighted standard deviation values, for the *P*- and *S*-wave velocity models, respectively, from the surface down to 200 km depth.

resulting weight sum maps at 20 and 30 km depth. E-supplement movies Mov1 and Mov2 show the variation of weight sums, for the *P*- and *S*-wave velocity models, respectively, from the surface down to 200 km depth. In general, the weight sum is higher for the mantle than for the crust. However, as mentioned above, because the crust and mantle models were built separately, their weight sums are not directly comparable. The higher weight sums in the mantle could seem counter-intuitive, considering that crustal models are usually associated with a finer-scale resolution. The difference in weights simply arises from the assignment of high weights to most mantle models (and comparatively lower weights to crustal models), as well as from their overall wider areal coverage. We delineated confidence limits for PRISM3D at all depths using an arbitrary weight-sum upper limit of 0.5 for the crust and 2.0 for the mantle, respectively.

We also computed the weighted standard deviation associated to the mean velocity field at each depth. This provides a quantitative estimate of the uncertainty arising from PRISM3D's input model variability. Fig. 6 presents the calculated standard deviation maps at 20 and 30 km depth, with values ranging in the crust from 0.15 to 0.5 km s^{-1} at 20 km and from 0.15 to 0.85 km s^{-1} at 30 km. At 20 km, the values with the highest variability are located offshore, which is also where the calculated weight sum is the lowest (see Fig. 5). The onshore part is characterized by comparatively lower standard deviation values (i.e. associated with lower variability), especially in the North, East and South of Iberia. At 30 km, standard deviation values higher than 0.4 km s^{-1} in the East of Iberia reveal a relative disagreement between the input models used in the compilation. In comparison to the crust, the calculated standard deviation appears much smaller in the mantle. This results partly from the fact that, at Moho depth and down to 60 km, mantle velocities are mostly constrained by the tomographic model of Díaz *et al.* (2013), as explained in the previous section. As a result, variability is low and so is the weighted standard deviation. Below 60 km depth, the calculated standard deviation ranges from 0.01 to 0.2 km s^{-1}, which is still lower than values observed in the crust, due to the mutual consistency between the mantle tomographic models used as inputs for PRISM3D, and also, to a certain extent, to the larger petrological homogeneity of the mantle with respect to that of the crust. E-supplement movies Mov3 and Mov4 show the evolution of weighted standard deviation with depth for V_P and V_S, respectively, from the surface down to 100 km depth. They show that V_P standard deviation tends to be higher than that of V_S, in absolute value, which does not necessarily mean that V_P is better constrained than V_S, since V_P is higher than V_S by a factor of 1.5–2.0. Both quantities show similar features, with a higher standard deviation offshore than onshore at crustal depths. The movies also confirm that mantle wave speed inputs show little variability, with weighted standard deviation values of the order of 0.1 km s^{-1} in the entire domain, at all depths.

4 RESULTS

4.1 Moho depth

Fig. 4 shows the depth of the crust–mantle boundary (Moho) in the PRISM3D model, which is ∼30–35 km over most of Iberia and ∼35–40 km in NW Africa. Higher Moho depth values and sharper Moho depth gradients are observed in NE Iberia and in the Gibraltar arc region. Those high Moho depth values are related to Alpine collision processes associated with the closure of the Tethys and opening of the Mediterranean domains (Rosenbaum *et al.* 2002). Fig. 7 shows cross-sections through the model. The Moho *a posteriori* mean depth and standard deviation are represented, along with the Moho depth input values from the literature and their *a posteriori* standard deviation inferred from the output of the Reversible Jump algorithm. It is worth noting that despite apparently strong gradients in the orogenic domains (in map view), the Moho depth surface is in fact relatively smooth and Moho depth gradients are not particularly sharp. It is clear, however, that the gradients in these domains contrast remarkably with the comparatively smoother Moho that characterizes the rest of the study area.

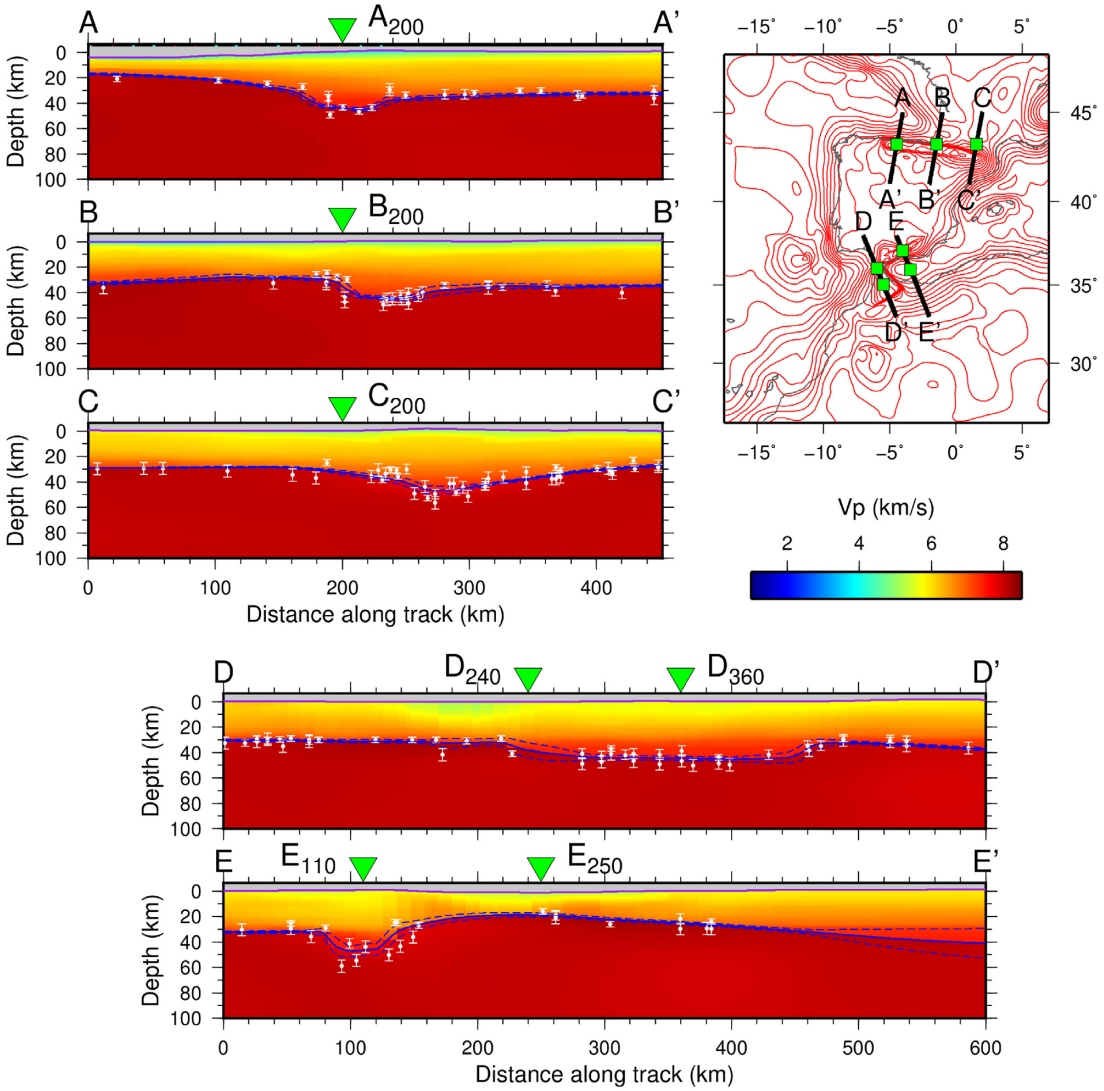

Figure 7. Cross-sections through PRISM3D *P*-wave speed structure across the Pyrenees (AA', BB' and CC') and the Betic-Rif system (DD' and EE'). The purple line represents topography and bathymetry, while the mean and one standard deviation interval inferred from the Moho depth posterior distribution are shown by the solid and dashed blue lines, respectively. The input Moho depth values (from receiver function and DSS studies) are also shown by the white circles with their associated error bars. Profile locations are indicated on the map in the upper right-hand corner. The red lines on the map are Moho depth isocontours, similar to those of Fig. 4(a). The green squares and inverted triangles, respectively on the map and along the profiles, indicate the locations where the Moho depth 1-D marginal posterior distributions represented on Fig. 8 were extracted. Note that the cross-sections horizontal and vertical axes are on the same scale, that is no vertical exaggeration was imposed.

As expected, regions with no Moho depth measurements show large errors (Fig. 4), with a posterior distribution tending towards the prior (EPcrust), hence meaning that no additional information was provided by Moho depth input models in those areas. Moho depth error is quite low over most of Iberia (<500 m), increasing to values of 2–4 km in the northern coast of Spain and in the Gibraltar region, where the Moho displays sharper gradients. Such high errors reflect both the amplitude of the Moho depth variations across the gradient and the uncertainty on the exact location of that gradient. It is important to note that the presence of a step in the Moho depth surface naturally produces large standard deviation estimates as it implies the presence of both high and low Moho depth values in its vicinity, on each side of the gradient. In such case, the posterior distribution is bimodal, with a Moho depth mean value that does not correspond to either the shallow nor the deep Moho but instead lies in between, and with a large standard deviation accounting for Moho depth variability across the step. Thus, Moho depths and gradients should be interpreted with caution in these regions. Fig. 8 shows the 1-D marginal posterior distribution of Moho depth at seven different locations in the Pyrenees and Betic-Rif area (A_{200}, B_{200}, C_{200}, D_{240}, D_{360}, E_{110} and E_{250}; their locations are given on Fig. 7). Marginal distributions at A_{200}, B_{200}, C_{200}, all three located in the Pyrenean range, show a gradual evolution from clearly bimodal to almost unimodal. The largest uncertainty is observed for B_{200}, where the two modes overlap. At A_{200},the two modes are well individualized, with a higher probability associated to the deeper mode, thus resulting in a mean shifted towards higher depths, and a lower standard deviation than that of B_{200}. Finally C_{200} is the least ambiguous of the three, with a nearly unimodal distribution and low standard deviation. Other unimodal (or close to unimodal) distributions can be seen for D_{360}, E_{110} and E_{250}, in the Betic-Rif region. D_{240},on the other hand, is an illustration of the complexity

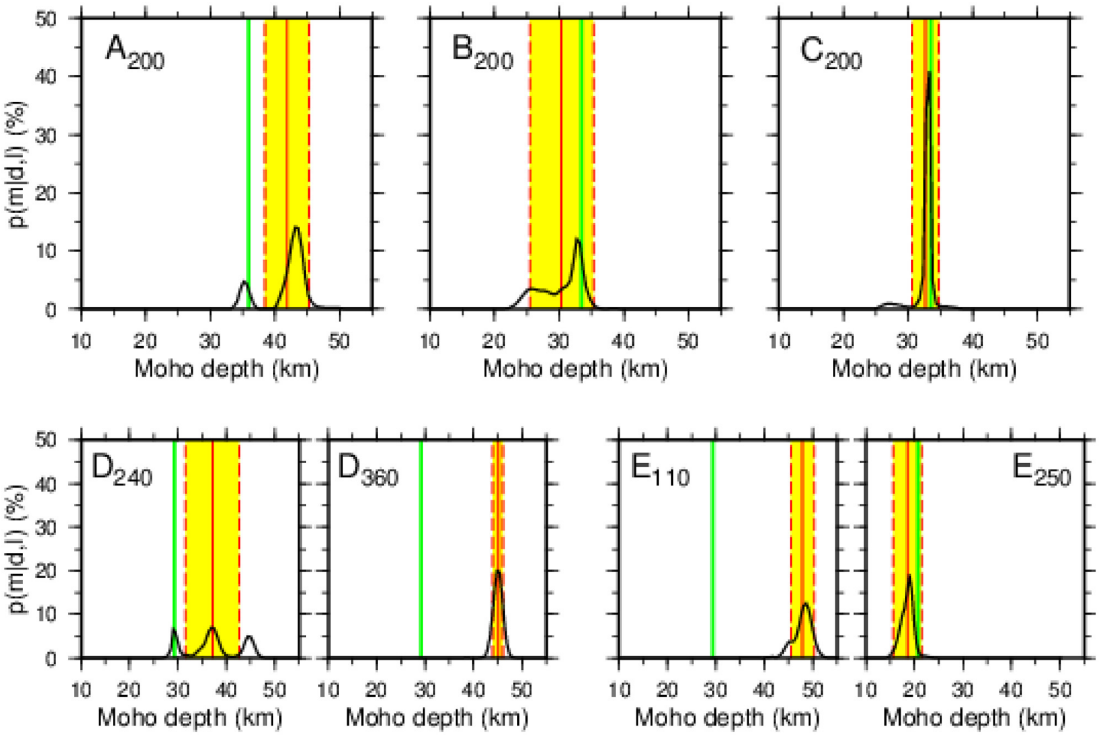

Figure 8. Examples of Moho depth 1-D marginal posterior probability distributions determined from the Reversible Jump algorithm output. Probabilities are shown in percent. A_{200}, B_{200}, C_{200}, D_{240}, D_{360}, E_{110} and E_{250} are the points where 1-D marginal distributions were extracted (see Fig. 7; subscripts are indicative of distance along the Moho depth profiles in Fig. 7, in km). Prior Moho depth at each location (mean of the uniform, prior distribution) is shown by the green line, while the mean posterior Moho depth is represented by the solid red line, along with its 1-standard deviation confidence interval (yellow box bounded by dashed red lines).

that can characterize the ensemble solution locally, in this case in the Gibraltar region, with a distribution showing three modes. Note that the coincidence of the prior mean value (represented in green) with secondary modes of the posterior distribution for A_{200} and D_{240} is fortuitous since the prior distribution is uniform and therefore does not show a peak at its mean. Those modes thus reflect the information contained in the data and are not due to any characteristics of the prior distribution.

With the exception of NW Morocco, Moho depth in north Africa is poorly constrained, in consequence of poor data coverage. Fig. 9 evidences the main differences between the Moho depth of PRISM3D (this study) and that of EPcrust (Molinari & Morelli 2011). In particular, PRISM3D includes: (1) a deeper Moho in NE Spain, including the Pyrenees (Mancilla & Diaz 2015); (2) a deeper Moho in the Gibraltar arc, a feature that is totally absent in EPcrust but is clearly imaged in recent studies (e.g. Fullea *et al.* (2010); Mancilla & Diaz (2015) and (3) a shallower Moho offshore SW Iberia, a feature that is also absent in EPcrust but clearly imaged by offshore active seismic experiments (Martínez-Loriente *et al.* 2014). This shallow Moho is due to mantle exhumation observed in the Gorringe Bank area, where the oceanic sediments lie directly on top of serpentinized mantle; as such it is not strictly speaking a Moho as it does not separate crust from mantle (crust is not present). In that part of the model the Moho should thus rather be considered simply as the top of the mantle. A comparison with the Moho depth surface model of Diaz *et al.* (2016) (Figs 9d–f), which was obtained with a similar input as that used in this work, shows that both models are consistent. The PRISM3D's Moho surface also tends to be deeper in the Pyrenees and in the Gibraltar arc region, and exhibits slightly sharper gradients.

4.2 *P* and *S* wave speed structure

Fig. 10 shows horizontal slices through the V_P and V_S structures of PRISM3D at 0, 5, 10, 20 and 30 km depth below sea level. It also shows the calculated V_P/V_S ratio at the same depths. That quantity should however be interpreted with caution as the V_P and V_S models from which it is determined do not necessarily have the same coverage nor resolution. E-supplements Mov5 and Mov6 show horizontal slices through the V_P and V_S structures of PRISM3D, down to 60 km below sea level, in steps of 0.5 km. In spite of detail differences, the first order features evidenced by the V_P and V_S structures are similar. The lowest seismic velocities, on the order $V_P \approx 2$ km s^{-1} and $V_S \approx 1$ km s^{-1}, are expectedly found at shallow depths in sedimentary domains, and more specifically in offshore basins. A very slow structure is also visible in northern Africa, in the southeastern part of the model, but in a region that is poorly covered by the input models that we used. The Iberian Massif appears characterized by fast seismic velocities in the top crust ($V_P \approx 5-6$ km s^{-1}, $V_S \approx 3$ km s^{-1}, at 0 km) and low V_P/V_S. V_P/V_S ratio values vary around 1.75, with values higher than average above 5 km depth in sedimentary domains. The V_P/V_S ratio appears more homogeneous in the deeper crust (from 10 km depth onwards) and in the mantle. The Betic-Rif system is quite clearly individualized from surrounding areas, with slightly lower V_P and V_S than average, as well as higher V_P/V_S, at all depths; that area being well covered by the input models, the feature is likely robust. Low V_P/V_S values, on the other hand, are visible on the 5 km slice in thinned crust regions, but these zones are all located at the periphery of the confidence region. Last, the 10-km slices on Fig. 10 show the exhumed mantle zone of the Gorringe Bank, offshore Portugal, in the southwestern part of the study area

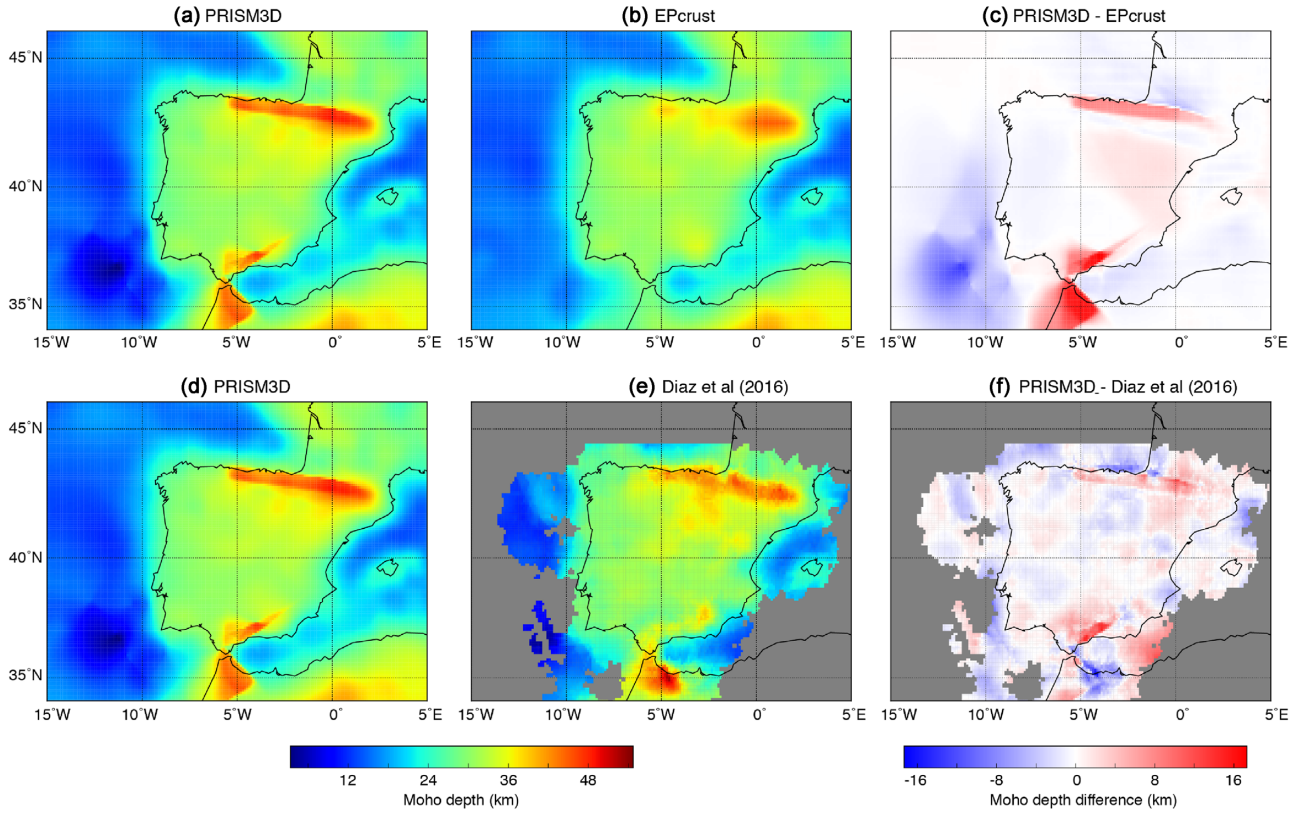

Figure 9. Moho depth in: (a, d) PRISM3D, (b) EPcrust, interpolated to the same 10-km horizontal spacing of PRISM3D, and (e) Diaz *et al.* (2016), also interpolated to the same 10-km horizontal spacing of PRISM3D. (c, f) Difference between the Moho depths of the PRISM3D and (c) EPcrust and (f) Diaz *et al.* (2016) models.

(see Fig. 1 for Gorringe Bank location). The deeper slices evidence the thinned crust domains of both the Atlantic and Mediterranean margins of Iberia, with a rather irregular crust mantle boundary on the Atlantic side on the 30 km slice.

Fig. 11 shows the evolution of the relative (with respect to the average velocity at each depth) *P* and *S* wave speed and calculated V_P/V_S ratio with depth in the upper mantle, from 50 to 200 km depth. The most prominent feature of these slices, on both V_P and V_S anomaly maps, is undoubtedly the well known arcuate high velocity anomaly attributed to a slab of oceanic lithosphere beneath the Alboran domain, which was imaged in different studies (Wortel & Spakman 2000; Bezada *et al.* 2013; Bonnin *et al.* 2014; Civiero *et al.* 2018, 2019). E-supplement movies Mov7 and Mov8 show the variation of the relative *P* and *S* wave speeds from 60 to 200 km, in steps of 5 km.

Fig. 12 shows cross-sections through the V_P structure of PRISM3D down to 60 km. E-supplements Mov9 and Mov10 show, respectively, NS and EW vertical cross-sections through the PRISM3D V_P structure. The cross-sections illustrate some of the main structural features described by PRISM3D, in particular Moho depth variations: (1) An elevated Moho, nearly reaching the surface, below the Gorringe bank (Fig. 12a,Martínez-Loriente *et al.* 2014); 2) An eastward dipping Moho, from ∼15 to ∼40 km below sea level, in the Cadiz and Gibraltar regions, followed by an abrupt thinning of the crust below the Alboran sea (Figs 12b, d and e, Sallarès *et al.* 2011; Mancilla & Diaz 2015) and (3) A thick crust below NE Spain (∼40 km), which becomes thicker (>40 km) below the Pyrenees. In the Pyrenees, the Moho dips gently from South to North, and then shallows abruptly on the north side of the mountain range (Figs 12c and g) (Mancilla & Diaz 2015). The elevated Moho below the Gorringe bank has been interpreted as indicating the presence of exhumed mantle (Martínez-Loriente *et al.* 2014). The dipping Moho surfaces below the Pyrenees and Gibraltar have been interpreted as lithosphere bending downwards as a consequence of convergence (Mancilla & Diaz 2015). In addition to Moho depth lateral variations, the cross-sections of Fig. 12 interestingly show the difference between areas that are well covered by tomographic models, such as the Betic-Rif domain (cross-sections C_1C_2, G_1G_2 and H_1H_2) or the Pyrenees (cross-section D_1D_2), where they reveal a certain degree of structural complexity, and those that are not, for instance the offshore domains visible on cross-section B_1B_2 or at both ends of cross-sections E_1E_2, F_1F_2, G_1G_2 and H_1H_2, where the layered structure of EPcrust is still visible.

4.3 Comparison with existing models

Fig. 13 compares the *P* wave speed values of PRISM3D with those from the recently published work of Lozano *et al.* (2020) at 5 and 30 km depth. Lozano *et al.* (2020) produced a 3-D *P* wave speed model for the Gulf of Cadiz and its surroundings, in the southwestern part of our study area. Their model results from the compilation of a large number of controlled-source seismic profiles that, in combination with 1-D generic profiles, were interpolated on a regular grid, with a 20 km × 20 km × 1 km node spacing. First order features from the two models are fairly similar, yet with a few slight differences.

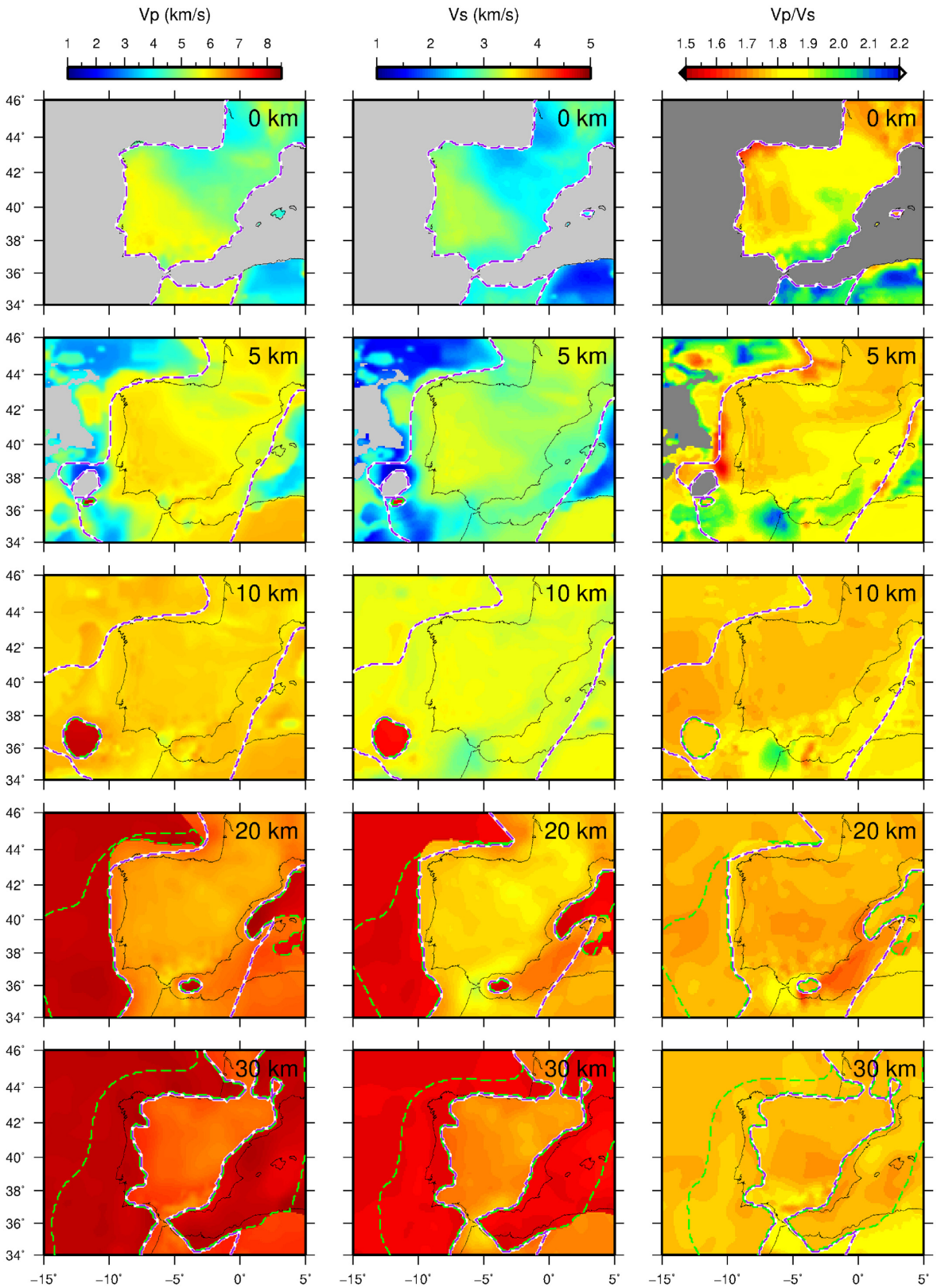

Figure 10. Crustal and subcrustal mantle V_P (left-hand panel), V_S (middle panel) and calculated V_P/V_S (right-hand panel) structure at depths of 0, 5, 10, 20 and 30 km. The 0.5 and 2.0 weight sum contour lines enclosing PRISM3D confidence region for the crust and mantle are shown as dashed purple and dashed green lines, respectively. E-supplements Mov5 and Mov6 show horizontal slices through the V_P and V_S structures of PRISM3D, down to 60 km below sea level, in steps of 1 km.

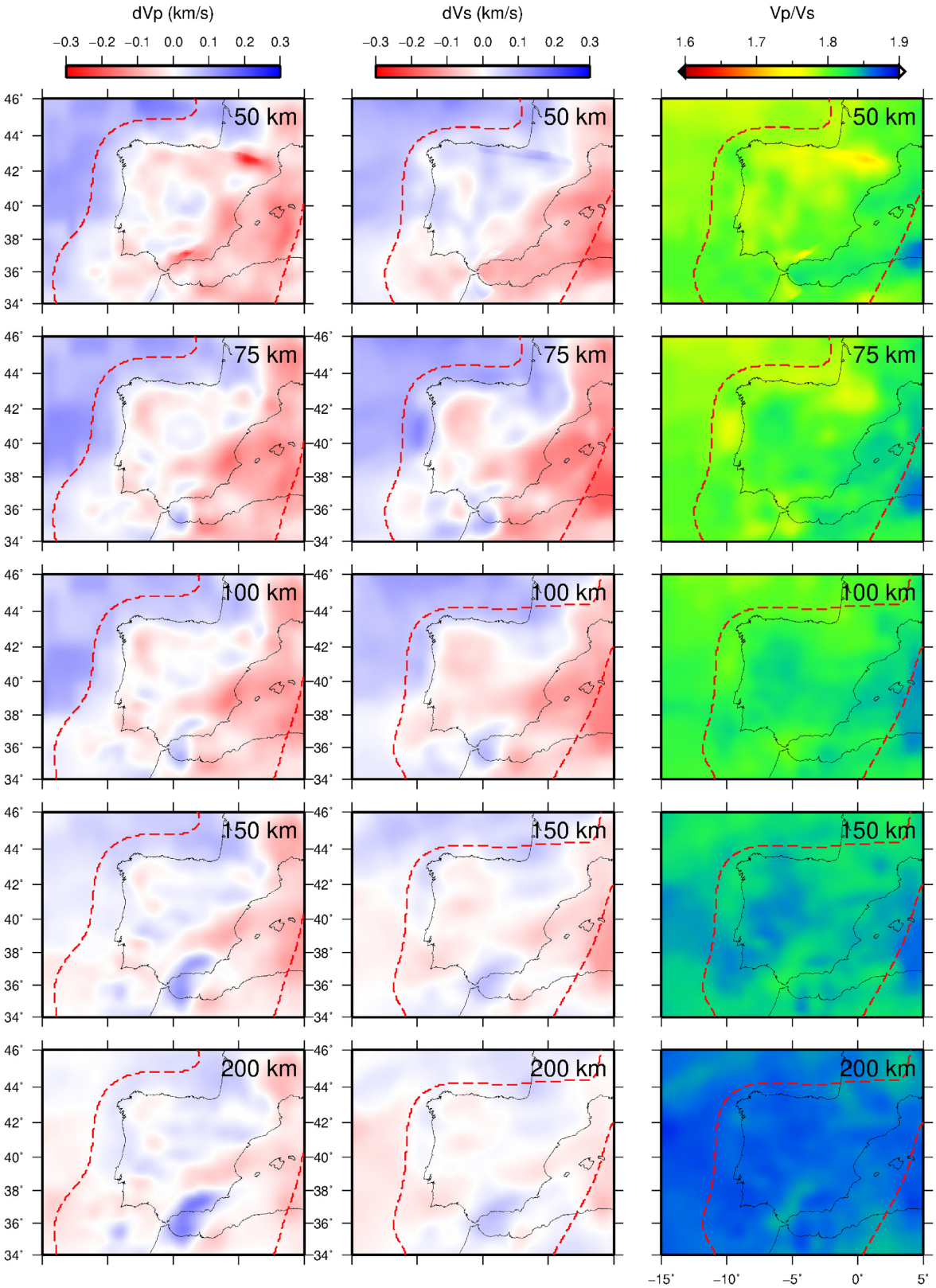

Figure 11. Mantle V_P (left-hand panel), V_S (middle panel) and calculated V_P/V_S (right-hand panel) structure at depths of 50, 75, 100, 150 and 200 km. Relative velocities are given with respect to the average velocity calculated at each depth. The 2.0 weight sum contour lines enclosing PRISM3D confidence region for the mantle are shown as dashed red lines. E-supplements Mov7 and Mov8 show horizontal slices through the V_P and V_S structures of PRISM3D in the mantle, from 60 to 200 km depth, in steps of 5 km.

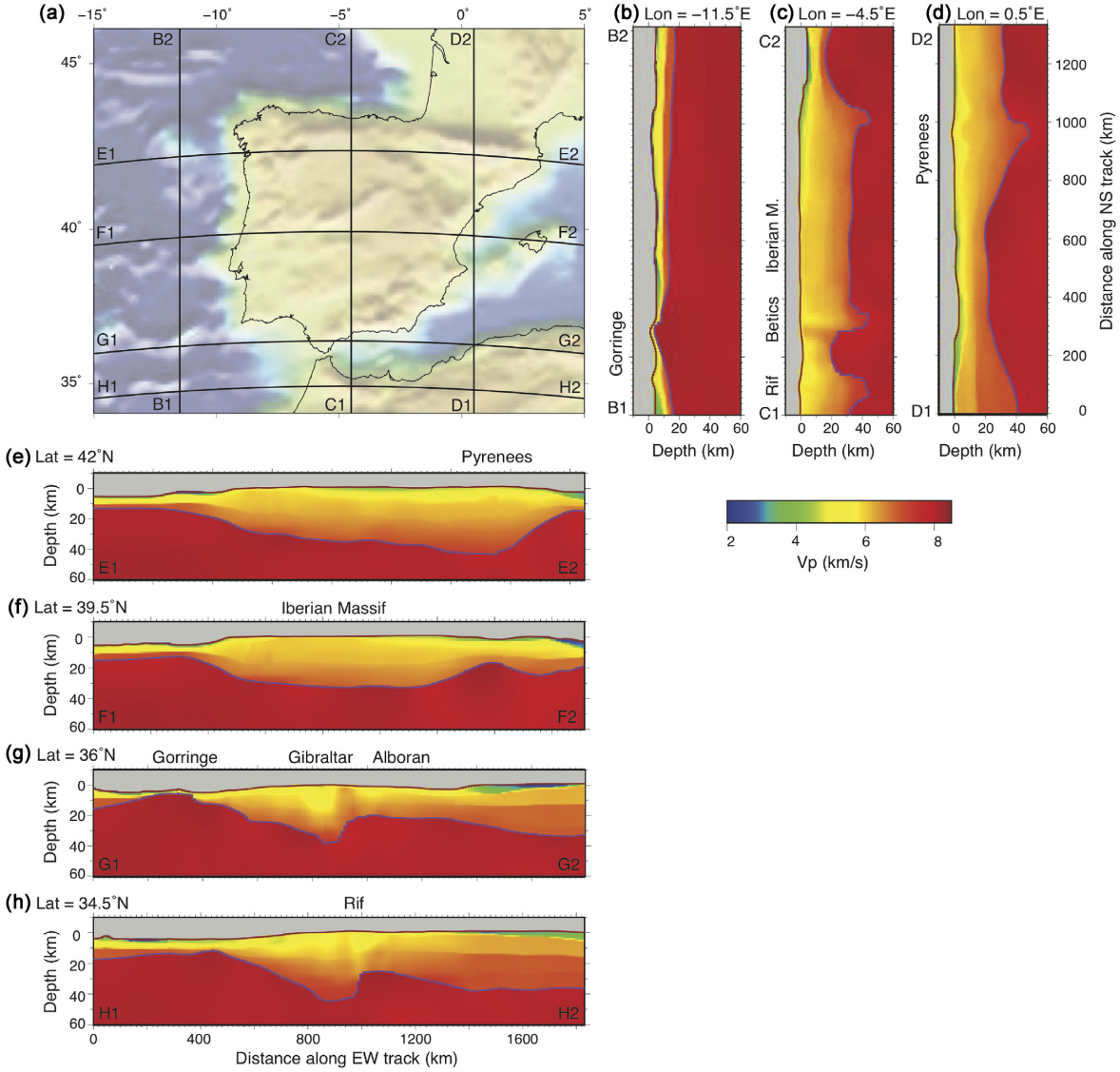

Figure 12. (a) Topographic and bathymetric map of Iberia (SRTM30+, Becker *et al.* 2009), showing NS cross-sections through the V_P structure of PRISM3D at longitudes of (b) –11.5°E, (C) –4.5°E and (C) 0.5°E, and EW cross-sections at latitudes of (E) 42°N, (F) 39.5°N, (G) 36°N and (H) 34°N. The vertical exaggeration of the cross-sections is ≈5. E-supplements Mov9 and Mov10 show, respectively, NS and EW vertical cross-sections through the PRISM3D V_P structure.

At 5 km depth, V_P is higher onshore than offshore in both models, with the lowest values found in the abyssal plains. At that depth, the clearest difference between the two models can be seen in the Gorringe Bank area, where high velocities in PRISM3D account for the presence of exhumed mantle evidenced from controlled-source seismic results (Martínez-Loriente *et al.* 2014). More details are visible in PRISM3D in southern Portugal and southwestern Spain, reflecting the level of detail of the tomographic models that were included in PRISM3D (Veludo *et al.* 2017; Silveira *et al.* 2016), but similar features can be identified in both, such as a clear low velocity patch on the Spanish side of the Gibraltar area corresponding to the western tip of the Guadalquivir basin. At 30 km, both models are also very similar, although Lozano *et al.* (2020) is smoother than PRISM3D. The overall shape of the crust–mantle boundary, which reveals the transition from east to west between thicker continental and thinner oceanic crust, however appears comparable, at first order, in both models.

On Fig. 14 we compare the crustal structure of PRISM3D with two profiles from a wide-angle reflection seismic experiment carried out in the South of our study area (Gil *et al.* 2014). Samples of Moho depth profiles from that experiment were part of the input Moho depth values used to build PRISM3D, as they were included in the compilation of Diaz *et al.* (2016). So, as expected, the crustal thicknesses are in fair agreement. The match, however, is not perfect, due to the presence of multiple data sets used as input to PRISM3D. Yet it is worth noting that this area corresponds to that covered by the profiles EE' and DD' on Fig. 7, where the good fit between the input Moho depths and those from PRISM3D is evident.

5 IMPACT ON TRAVELTIMES

In this section, we compare the traveltimes predicted by PRISM3D and by a 1-D layered model commonly used in the region. Fig. 15 shows the 1-D profile obtained by laterally averaging V_P and V_P/V_S

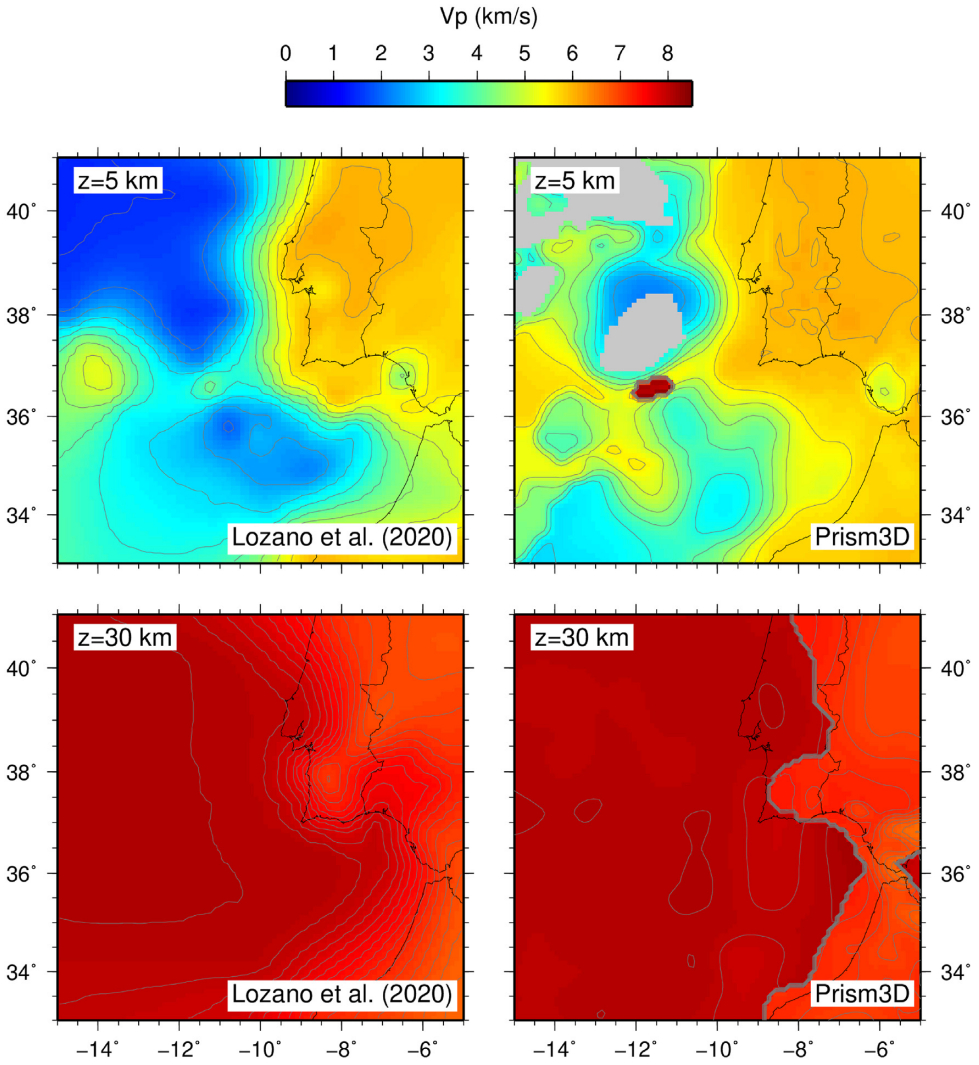

Figure 13. Comparison of PRISM3D (right-hand panel) with the model of Lozano *et al.* (2020) (left-hand panel) at 5 km (top panel) and 30 km depth (bottom panel). Contour lines are drawn every 0.5 km s^{-1} at 5 km and every 0.1 km s^{-1} at 30 km. In PRISM3D, the concentration of contour lines at the crust–mantle boundary visible on the 30-km-slice evidences the sharper velocity contrast in PRISM3D than in Lozano *et al.* (2020) across that interface.

values at each depth in PRISM3D, along with its standard deviation. The figure also shows the 1-D V_P and V_P/V_S profiles of model IGN, which is routinely used by Instituto Português do Mar e da Atmosfera (IPMA) to locate earthquakes in Iberia (Custódio *et al.* 2015). The IGN model has a fixed $V_P/V_S = 1.75$. In comparison to the IGN 1-D model, the 1-D, depth-averaged PRISM3D model portrays a slower upper crust, down to ∼10 km, and a slightly faster lower crust, between ∼10 and 30 km depth. Both models have similar velocities in the uppermost mantle (∼30–90 km), with IGN being slightly slower than PRISM3D, on average. The IGN 1-D model shows a sharp step increase in seismic velocities at a depth of ∼90 km, whereas PRISM3D shows a progressive increase of seismic velocities from ∼120 km down to 200 km. Due to the high V_P/V_S ratio values in sedimentary basins, the average V_P/V_S is relatively higher for PRISM3D in the top 5 km, decreasing to an average value of about 1.75 at ∼10 km depth, similar to that of IGN. V_P/V_S then increases in the mantle up to a value of about 1.84 at 200 km depth, following the AK135 model (Kennett *et al.* 1995).

We used NonLinLoc (Lomax *et al.* 2000) to forward compute the traveltimes of the first arriving *P* and *S* waves through the PRISM3D and IGN models in a fully 3-D volume. We first placed a synthetic hypocentre in the approximate centre of Iberia, at 4.5°W, 40°N and 10 km depth (Fig. 16a). We discretized the study region using grid nodes spaced 1 km apart, both horizontally and vertically. In order to minimize geometric distortion due to the projection of the spherical real Earth onto the cubic NonLinLoc grid, we used a Transverse Mercator projection centred at the synthetic epicentre. Nevertheless, due to the flat Earth approximation the 3-D grid can only propagate traveltimes accurately at local to regional distances (Snoke & Lahr 2001). We then computed theoretical traveltimes for stations along ∼500-km-long profiles, starting at the synthetic epicentre and extending along different azimuths, from 0° (NS profile) to 330°, in steps of 30° (Fig. 16a). Fig. 16(c) shows the difference between the theoretical traveltimes predicted using the layered IGN and the PRISM3D models, for the first *P*-wave arrival, along the northward profile (azimuth=0°), as well as surface and Moho topographies along the same profile. Fig. 16 evidences the impact of a laterally varying seismic structure on the predicted traveltimes. In continental Iberia, PRISM3D is slower than IGN at upper crustal levels. This results in later P_g arrival times predicted by PRISM3D with respect to those predicted by IGN. The traveltime difference between models increases up to the P_g–P_n cross-over distance, at ∼120 km from

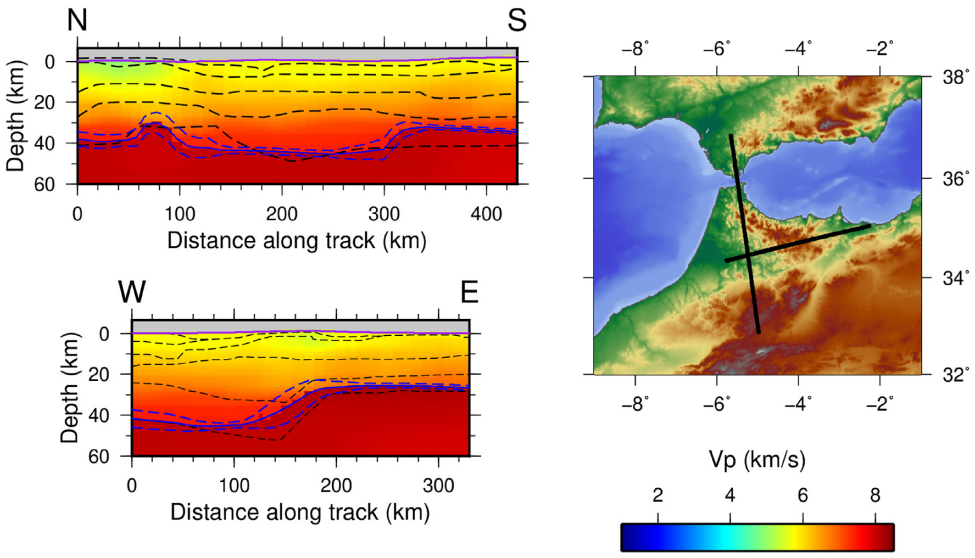

Figure 14. Comparison of PRISM3D's *P*-wave speed structure with that from Gil *et al.* (2014). The location of the two profiles is given on the map on the right, while the north–south and east–west profiles are shown on the top and bottom left, respectively. On the profiles, PRISM3D's Moho depth surface is represented by the blue solid line, along with its associated one standard deviation interval (dashed blue line). Interfaces from Gil *et al.* (2014) are shown by the black dashed lines.

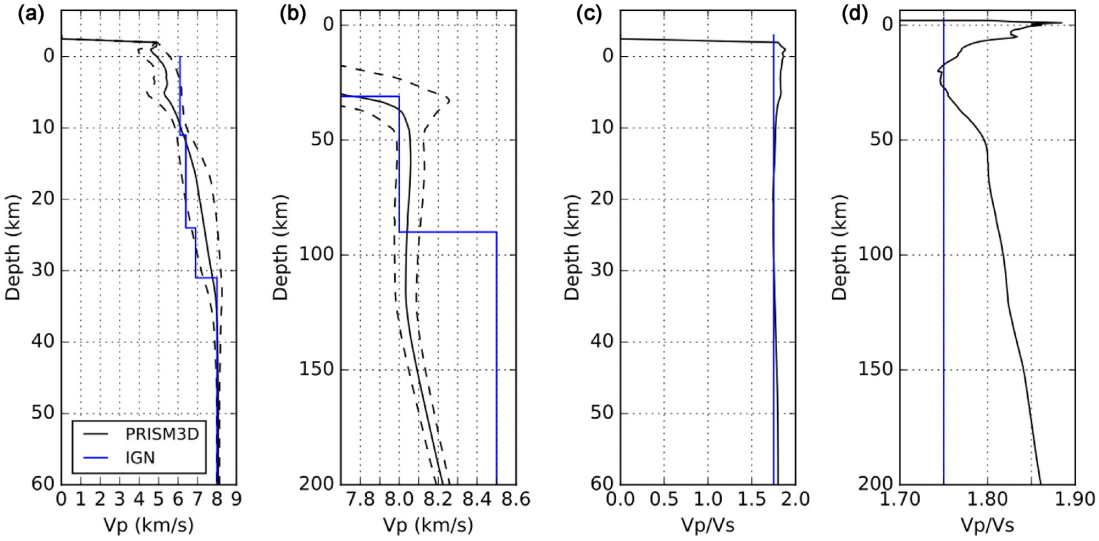

Figure 15. Comparison between the lateral average of PRISM3D (black) and the 1-D model IGN (blue), used by IPMA to routinely locate earthquakes in Iberia (Custódio *et al.* 2015). V_P vertical profiles down to depths of (a) 60 km, and (b) 200 km. The standard deviation of the PRISM3D model is indicated by dashed black lines. (c) and (d) V_P/V_S vertical profiles down to depths of 60 km, and 200 km, respectively.

the epicentre. Fig. 17 shows the reduced traveltimes, considering a velocity of 8 km s^{-1}, for the PRISM3D and IGN models along all cross-sections. The figure shows that the cross-over distance for the NS profile is shorter when using PRISM3D than when using the IGN model. Then, the traveltime difference between the two models stays broadly constant up to ∼300 km of epicentral distance, where PRISM3D becomes again slower due to the thickening of the crust in northern Iberia. Finally, the PRISM3D traveltimes decrease dramatically with respect to IGN from ∼400 km onwards: The Moho shallows significantly, and PRISM3D becomes faster than IGN due to longer ray paths within the mantle. At such distances, rays travel in the uppermost part of the mantle. As a result, the traveltimes calculated with the IGN 1-D model are not affected by the strong V_P increase at 90 km depth and below, which would result, at larger distances, in faster *P* waves in the IGN model than in PRISM3D. These patterns are persistent for most profiles, both for *P* and *S* waves (Figs 16 e and g, respectively).

Figs 16(b), (d), (f) and (h) show a similar computation to that just described above, showing traveltime differences between IGN1D and PRISM3D along the same profiles discussed before. However, the epicentres are now placed at the outer edge of each cross-section rather than at the centre of Iberia (Fig. 16b). This example is more representative of what we observe in the real Earth, as many of the earthquakes recorded in Iberia are located at its edges. Along the northwards profile (azimuth=0°), PRISM3D is initially slower, in consequence of the shallow sediment layer. However, at ∼50 km along profile there is an inversion of this tendency, and PRISM3D starts to become faster, in result of the shallower offshore

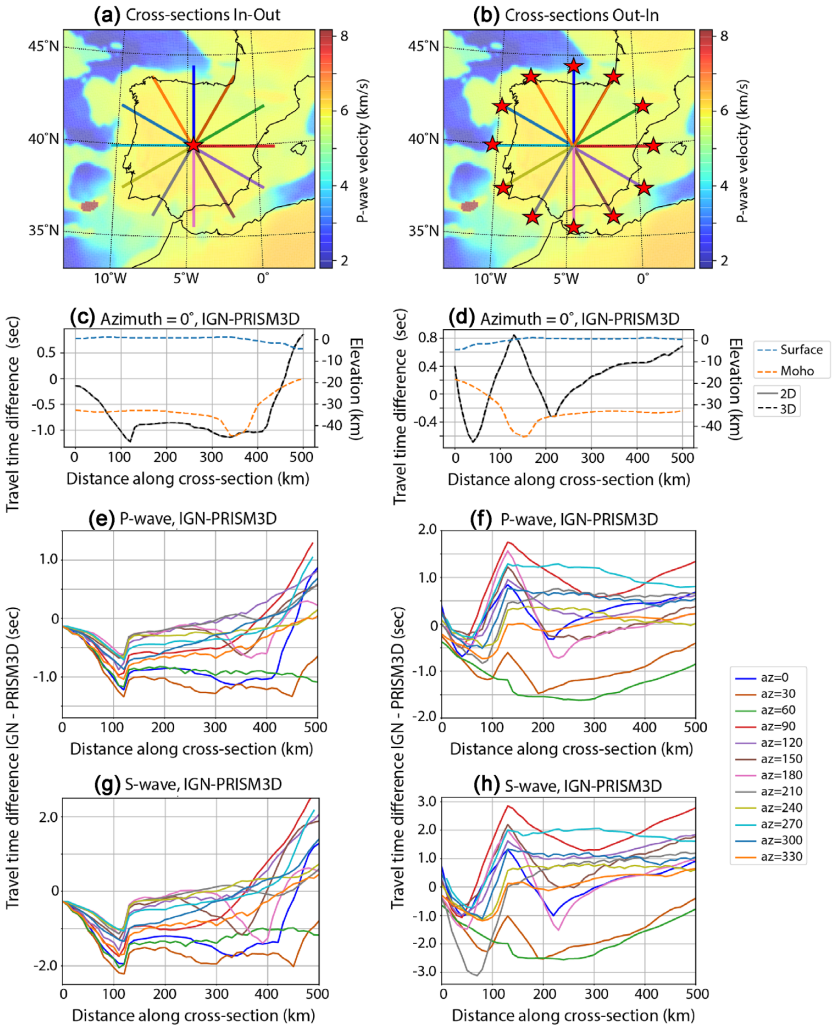

Figure 16. Differences between the traveltimes predicted by the 1-D IGN and the PRISM3D models. (a) Profiles along which traveltimes were computed, starting at a synthetic epicentre in the centre of Iberia (4.5°W, 40°N, 10 km depth). The azimuthal interval between profiles is 30°. The background shows the *P*-wave velocity of PRISM3D at a depth of 5.5 km. (b) Same as A, but now the epicentres are placed at the edge of Iberia, at 500 km distance from the chosen point at the centre of Iberia (4.5°W, 40°N, 10 km depth). (c) Difference between the *P*-wave traveltimes predicted by the 1-D IGN model and PRISM3D, along the northwards profile, that is, azimuth=0°, considering the epicentre at the centre of Iberia and forward computing the traveltimes in a 3-D volume (dashed black line). The results are similar if the traveltimes are computed using a 2-D structure corresponding to a cross-section of the 3-D volume (solid grey line).. The topography of the surface (dashed blue line) and of the Moho (dashed orange line) along the profile are also shown. (d) Same as C, but with the synthetic epicentre placed at the edge of Iberia. (e) Differences between the *P*-wave traveltimes predicted by the 1-D IGN and PRISM3D models, considering the epicentre at the centre of Iberia, along profiles whose azimuths are spaced 30°. The legend of the figure shows the azimuths of the profiles, colour-coded as in (a). (f) Same as (e), but with the synthetic epicentre placed at the edge of Iberia. (g, h) Same as (e, f) but for *S* waves. The differences in traveltimes between the traveltimes predicted by 1-D IGN and PRISM3D model with respect to azimuth for a source located at the centre and at the edge of Iberia, respectively, is illustrated in supplementary material Mov11 and Mov12 for *P* waves, and Mov13 and Mov14 for *S* waves.

Moho and propagation of seismic waves in the faster upper mantle. This tendency is again inverted at ∼120 km, when the Moho in PRISM3D becomes deeper than that of IGN1D, and PRISM3D starts to become slower again due to longer ray paths in crustal material. In general, there is a stronger variability in traveltime differences between IGN1D and PRISM3D when the hypocentre is placed at the outer edge of the cross-sections. This results from the stronger lateral variation of the Earth's structure close to the hypocentre.

The traveltime differences between IGN and PRISM3D, considering all azimuths, varies approximately between approximately –1.5 and 1.5 s for the first *P*-wave arrival, and between –2.5 and 2.5 s for the first-arriving *S* wave (Figs 16e–h). For visualization purpose, supplementary material Mov11 and Mov12 show the differences between theoretical traveltimes predicted using the 1-D IGN and the PRISM3D models, for the first *P*-wave arrivals, along profiles with azimuths spaced 1° apart and with the epicentre at the centre of Iberia and at the outer edge of the cross-section, respectively. Supplementary material Mov13 and Mov14 show the same but for *S*-wave traveltimes. In order to speed up computations, the movies do not show the results of full 3-D wave propagation, but rather the propagation of rays through 2-D cross-sections of PRISM3D corresponding to the chosen profile. Traveltimes computed using a full 3-D volume (dashed black line in Figs 16c–d) and 2-D cross-sections (grey line in Figs 16c–d) are in general good agreement, showing the same features.

Because PRISM3D describes the laterally varying seismic structure of Iberia, it is expected to improve seismological studies in the

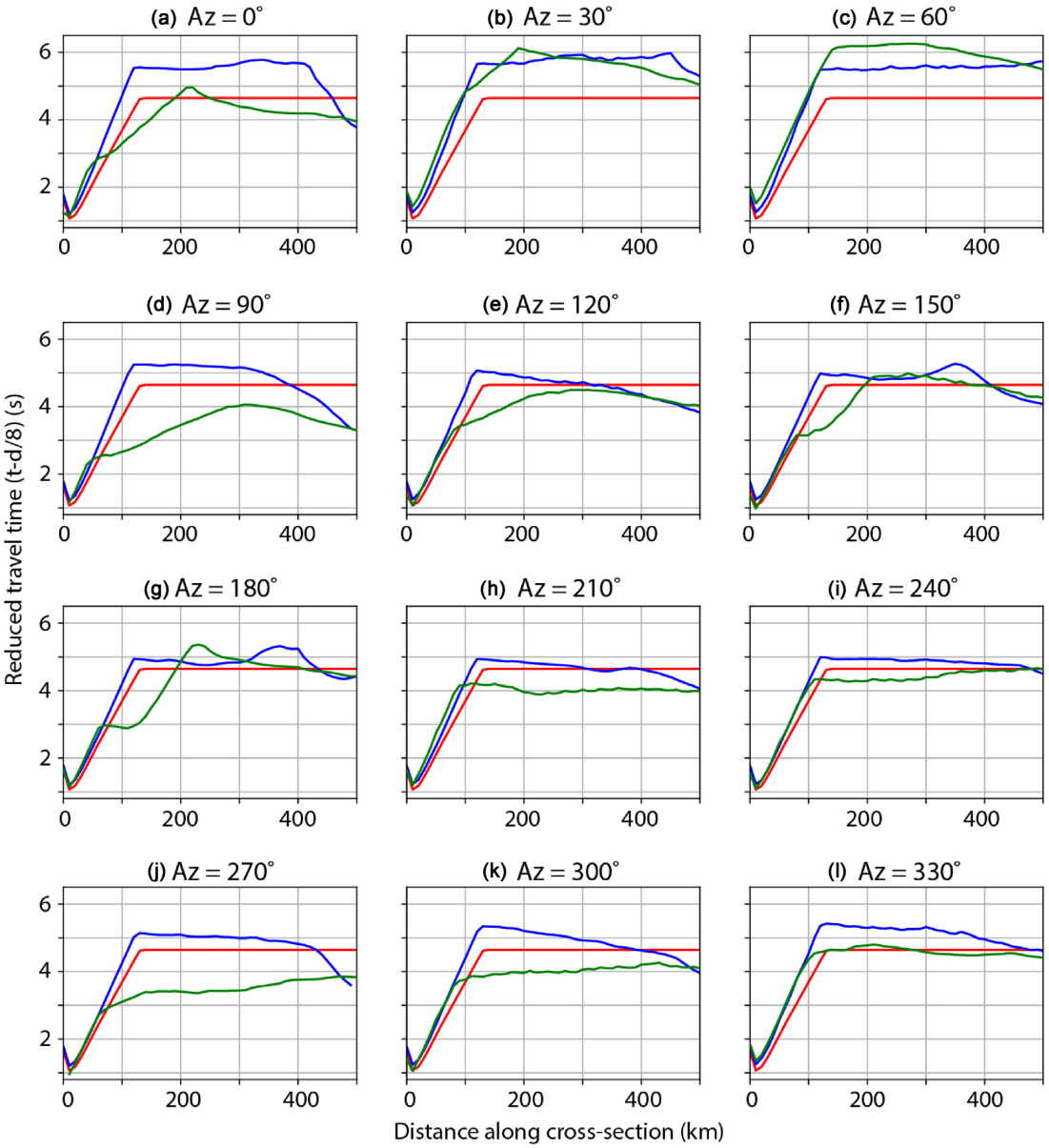

Figure 17. Reduced traveltime plots for the 12 profiles shown on Fig. 16, computed using the 1-D IGN model (red) and PRISM3D both with the epicentre placed in the centre (blue) and at the edge (green) of Iberia. (a–l) Cross-sections with azimuths varying between 0° and 330° in steps of 30°. When the epicentre is placed at the centre of Iberia, the PRISM3D model is consistently slower on all profiles, although at long distances (∼400 km) it becomes faster on profiles showing thinned crust due to the continent–ocean transition. The Pg–Pn cross-over distance is shorter with PRISM3D, which explains the sharp increase in traveltime difference that can be observed at ∼120 km on Figs 16(e) and (f). The variability in traveltimes with azimuth is much stronger when the epicentre is placed at the edge of Iberia, as a result of strong Earth structure heterogeneity close to the hypocentre.

region. This has been exemplified in a previous study of seismicity in Alentejo (southern Portugal) by Matos *et al.* (2018). This study showed that epicentral locations calculated with PRISM3D, using NonLinLoc to compute traveltimes on a full 3-D grid, could be shifted by up to ∼10 km with respect to those obtained with the IGN 1-D model. In addition, the authors showed that the locations obtained using PRISM3D displayed better quality indicators with respect to those obtained with the IGN layered model, namely lower average location errors and lower differences between expected and maximum-likelihood hypocentre. An important feature of PRISM3D is the explicit definition of surface topography and Moho depth surface, which potentially allows the simultaneous use of crustal phases and waves refracted along the crust–mantle boundary if both are observed at a given seismic station. The model has also been advantageously used as a starting model for teleseismic mantle tomography below Iberia, where it allowed to reduce the influence of unmodelled crustal structure and to initiate the inversion with a more accurate starting model (e.g. Civiero *et al.* 2018, 2019).

6 DISCUSSION AND CONCLUSIONS

We used the wealth of new seismic models available for Iberia and adjacent areas, which result from a strong instrumentation effort carried out in recent decades, in order to build a unified 3-D earth

model for Iberia—PRISM3D. PRISM3D approximates the real 3-D Earth's structure by describing two interfaces with topography—surface and Moho—and by describing the lateral and vertical variations of *P* and *S* wave speeds within both the crust and the mantle, down to 200 km. Uncertainty estimates, in the form of calculated standard deviation on both Moho depth and wave speed values, are also provided, thus allowing to assess the reliability of the model at any point of the grid.

Main features of PRISM3D include:

(1) a thick crust below NE Spain (∼40 km), which becomes thicker (>40 km) below the Pyrenees. In the Pyrenees, the Moho dips gently from south to north, and then shallows abruptly on the north side of the mountain range (Figs 12c and g, Mancilla & Diaz 2015);
(2) an eastward dipping Moho, from ∼15 to ∼40 km depth, in the Cadiz and Gibraltar regions, followed by an abrupt thinning of the crust below the Alboran sea (Figs 12b, d and e, Fullea *et al.* 2010; Sallarès *et al.* 2011; Mancilla & Diaz 2015);
(3) an elevated Moho, nearly reaching the surface, below the Gorringe bank (Fig. 12a, Martínez-Loriente *et al.* 2014), and (4) a smooth, almost planar Moho beneath the Iberian Massif.

In comparison to the 1-D IGN model, which is commonly used by IPMA to locate earthquakes, PRISM3D portrays a slower upper crust (down to ∼10 km), a slightly faster lower crust (∼10–30 km) and a faster uppermost mantle. PRISM3D also shows a progressive increase of seismic velocities from ∼120 200 km depth, whereas the 1-D IGN model shows a sharp step increase in seismic velocities at a depth of ∼90 km. Accordingly, traveltime comparisons show that PRISM3D is slower at upper crustal levels than IGN in continental Iberia, which results in later arrival time predictions when using PRISM3D. At the edges of continental Iberia, the Moho shallows significantly, causing large traveltime differences between IGN and PRISM3D, with PRISM3D becoming comparatively faster. Calculated traveltime differences between the two models at epicentral distances ranging from 0 to 500 km, vary from –1.5 to 1.5 s for *P* waves and from –2.5 and 2.5 s for *S* waves, which is much larger than typical phase picking errors. The variability in traveltimes with azimuth is much stronger when the epicentre is placed at the edge of Iberia, as a result of strong Earth structure heterogeneities close to the hypocentre. Such high traveltime differences are expected to have a strong impact on earthquake location in the region. PRISM3D can readily be used to characterize hypocentral parameters with 3-D earthquake location software (e.g. Lomax *et al.* 2000). It can also serve as a starting model for local earthquake tomography, and to apply crustal corrections in mantle tomography studies.

ACKNOWLEDGEMENTS

Constructive reviews from two anonymous reviewers and the Associated Editor greatly improved the quality of this paper. We are also indebted to all authors who generously provided their models to this compilation. Fruitful discussions with Manel Prada about mantle exhumation in the Gorringe Bank helped clarify the text, and significant improvements of this work were made possible thanks to insightful comments expressed by Ian Main and John Douglas in the framework of Sigma-2 Research Programme. This publication is supported by the FCT project SPIDER - Seismogenic processes in slowly deforming regions (PTDC/GEO-FIQ/2590/2014). The work presented is a contribution to FCT UIDB/50019/2020 IDL. P. Arroucau acknowledges support from Science Foundation Ireland (grant 13/CDA/2192) and from the Geological Survey of Ireland (grant 2016-PD-06). C. Civiero was supported by the Science Foundation Ireland, the Geological Survey of Ireland, and the Marine Institute (grants 13/CDA/2192 and 16/IA/4598). Figures were plotted using the GMT - Generic Mapping Tools software (Wessel & Smith 1998) and Python Matplotlib and Basemap packages. NonLinLoc was used for the forward computation of arrival times (Lomax *et al.* 2000). We also wish to thank Catarina Matos for the tests she performed on an early version of the model.

REFERENCES

Afilhado, A., Matias, L., Shiobara, H., Hirn, A., Mendes-Victor, L. & Shimamura, H., 2008. From unthinned continent to ocean: the deep structure of the West Iberia passive continental margin at 38°N, *Tectonophysics,* **458**(1–4), 9–50.

Albuquerque Seismological Laboratory (ASL)/USGS, 1988. Global Seismograph Network - IRIS/USGS, International Federation of Digital Seismograph Networks, doi:10.7914/SN/IU.

Amante, C. & Eakins, B., 2009. Etopo1 1 arc-minute global relief model: procedures, data sources and analysis., Tech. rep., NOAA Technical Memorandum NESDIS NGDC-24. National Geophysical Data Center, NOAA.

Amaru, M., 2007. Global traveltime tomography with 3D reference models, *Geol. Ultraiectina,* **274**.

Andrs, J., Draganov, D., Schimmel, M., Ayarza, P., Palomeras, I., Ruiz Fernandez, M. & Carbonell, R., 2019. Lithospheric image of the central Iberian zone (Iberian massif) using global-phase seismic interferometry, *Solid Earth,* **10,** 1937–1950.

Ayarza, P. *et al.*, 2014. Crustal thickness and velocity structure across the Moroccan atlas from long offset wide-angle reflection seismic data: the SIMA experiment, *Geochem. Geophys. Geosyst.,* **15**(5), 1698–1717.

Basili, R. *et al.*, 2013. The European Database of Seismogenic Faults (EDSF) compiled in the framework of the Project SHARE, http://diss.rm.ingv.it/share-edsf/, doi:10.6092/INGV.IT-SHARE-EDSF.

Batista, L., Hübscher, C., Terrinha, P., Matias, L., Afilhado, A. & Lüdmann, T., 2017. Crustal structure of the Eurasia–Africa plate boundary across the Gloria fault, north Atlantic ocean, *Geophys. J. Int.,* **209**(2), 713–729.

Becker, J.J. *et al.*, 2009. Global bathymetry and elevation data at 30 arc seconds resolution: SRTM30+, *Mar. Geod.,* **32**(4), 355–371.

Bezada, M., Humphreys, E., Toomey, D., Harnafi, M., Dávila, J. & Gallart, J., 2013. Evidence for slab rollback in westernmost Mediterranean from improved upper mantle imaging, *Earth planet. Sci. Lett.,* **368**(0), 51–60.

Bezada, M.J., Humphreys, E.D., Davila, J.M., Carbonell, R., Harnafi, M., Palomeras, I. & Levander, A., 2014. Piecewise delamination of Moroccan lithosphere from beneath the Atlas Mountains, *Geochem. Geophys. Geosyst.,* **15,** 975–985.

Bird, P., 2003. An updated digital model of plate boundaries, *Geochem. Geophys. Geosyst.,* **4**(3), doi:10.1029/2001GC000252.

Bodin, T., Salmon, M., Kennett, B.L.N. & Sambridge, M., 2012. Probabilistic surface reconstruction from multiple data sets: an example for the Australian Moho, *J. geophys. Res.,* **117,** B10307.

Bonnin, M., Nolet, G., Villaseñor, A., Gallart, J. & Thomas, C., 2014. Multiple-frequency tomography of the upper mantle beneath the African/Iberian collision zone, *Geophys. J. Int.,* **198**(3), 1458–1473.

Béthoux, N. *et al.*, 2016. Earthquake relocation using a 3D a-priori geological velocity model from the western Alps to Corsica: implication for seismic hazard, *Tectonophysics,* **670,** 82–100.

Cabral, J., 2012. Neotectonics of mainland Portugal: state of the art and future perspectives, *J. Iberian Geol.,* **38**(1), doi:10.5209/rev_JIGE.2012.v38.n1.39206.

Chen, H., Chiu, J.-M., Pujol, J., Kim, K.-H., Chen, K.-C., Huang, B.-S., Yeh, Y.-H. & Chiu, S.-C., 2006. A simple algorithm for local earthquake location using 3D Vp and Vs models: test examples in the central United States and in central eastern Taiwan, *Bull. seism. Soc. Am.,* **96,** 288–305.

Chevrot, S., Sylvander, M., Diaz, J., Ruiz, M. & Paul, A., Pyrope Working Group, 2015. The Pyrenean architecture as revealed by teleseismic P-to-S converted waves recorded along two dense transects, *Geophys. J. Int.,* **200,** 1096–1107.

Chevrot, S. *et al.*, 2014. High-resolution imaging of the Pyrenees and Massif Central from the data of the PYROPE and IBERARRAY portable array deployments, *J. geophys. Res.,* **119,** 6399–6420.

Civiero, C., Custdio, S., Duarte, J.C., Mendes, V.B. & Faccenna, C., 2020. Dynamics of the Gibraltar arc system: a complex interaction between plate convergence, slab pull, and mantle flow, *J. geophys. Res.,* **125**(7), e2019JB018873.

Civiero, C., Custodio, S., Rawlinson, N., Strak, V., Silveira, G., Arroucau, P. & Corela, C., 2019. Thermal nature of mantle upwellings below the Ibero-Western Maghreb region inferred from teleseismic tomography, *J. geophys. Res.,* **124**(2), 1781–1801.

Civiero, C., Strak, V., Custódio, S., Silveira, G., Rawlinson, N., Arroucau, P. & Corela, C., 2018. A common deep source for upper-mantle upwellings below the Ibero-western Maghreb region from teleseismic P-wave traveltime tomography, *Earth planet. Sci. Lett.,* **499,** 157–172.

Custódio, S., Lima, V., Vales, D., Cesca, S. & Carrilho, F., 2016. Imaging active faulting in a region of distributed deformation from the joint clustering of focal mechanisms and hypocentres: application to the Azores–Western Mediterranean region, *Tectonophysics,* **676,** 70–89 .

Custódio, S. *et al.*, 2014. Ambient noise recorded by a dense broadband seismic deployment in Western Iberia, *Bull. seism. Soc. Am.,* **104**(6), 2985–3007.

Custódio, S. *et al.*, 2015. Earthquakes in western Iberia: improving the understanding of lithospheric deformation in a slowly deforming region, *Geophys. J. Int.,* **203**(1), 127–145.

de Lamotte, D.F., Leturmy, P., Missenard, Y., Khomsi, S., Ruiz, G., Saddiqi, O., Guillocheau, F. & Michard, A., 2009. Mesozoic and Cenozoic vertical movements in the atlas system (Algeria, Morocco, Tunisia): an overview, *Tectonophysics,* **475**(1), 9–28.

DeMets, C., Gordon, R.G. & Argus, D.F., 2010. Geologically current plate motions, *Geophys. J. Int.,* **181**(1), 1–80.

de Vicente, G. & Vegas, R., 2009. Large-scale distributed deformation controlled topography along the western Africa–Eurasia limit: tectonic constraints, *Tectonophysics,* **474**(1–2), 124–143.

Dias, N., Silveira, G. & Haberland, C., 2010. Data of the temporary seismic WILAS network, GFZ Data Services, doi:10.14470/3N7565750319.

Diaz, J., Gallart, J. & Carbonell, R., 2016. Moho topography beneath the Iberian-western Mediterranean region mapped from controlled-source and natural seismicity surveys, *Tectonophysics,* **692**(Part A), 74–85.

Duarte, J.C., Rosas, F.M., Terrinha, P., Gutscher, M.-A., Malavieille, J., Silva, S. & Matias, L., 2011. Thrust–wrench interference tectonics in the Gulf of Cadiz (Africa–Iberia plate boundary in the North-East Atlantic): insights from analog models, *Mar. Geol.,* **289**(1–4), 135–149.

Díaz, J. & Gallart, J., 2009. Crustal structure beneath the Iberian Peninsula and surrounding waters: a new compilation of deep seismic sounding results, *Phys. Earth planet. Inter.,* **173**(1–2), 181–190.

Díaz, J., Gallart, J., Córdoba, D., Senos, L., Matias, L., Suriñach, E., Hirn, A. & Maguire, P., 1993. A deep seismic sounding investigation of lithospheric heterogeneity and anisotropy beneath the Iberian Peninsula, *Tectonophysics,* **221**(1), 35–51.

Díaz, J., Gil, A. & Gallart, J., 2013. Uppermost mantle seismic velocity and anisotropy in the Euro-Mediterranean region from Pn and Sn tomography, *Geophys. J. Int.,* **192,** 310–325.

Díaz, J. *et al.*, 2010. Background noise characteristics at the IberArray broadband seismic network, *Bull. seism. Soc. Am.,* **100**(2), 618–628.

Dündar, S., Dias, N.A., Silveira, G., Kind, R., Vinnik, L., Matias, L. & Bianchi, M., 2016. Estimation of the crustal bulk properties beneath mainland Portugal from P-wave teleseismic receiver functions, *Pure appl. Geophys.,* **173,** 1949–1970.

Ehsan, S.A. *et al.*, 2015. Lithospheric velocity model across the southern central Iberian zone (Variscan Iberian massif): the Alcudia wide-angle seismic reflection transect, *Tectonics,* **34**(3), 535–554.

El Moudnib, L. *et al.*, 2015. Crustal structure of the BETIC–RIF system, western Mediterranean, from local earthquake tomography, *Tectonophysics,* **643**(Supplement C), 94–105.

Faccenna, C., Piromallo, C., Crespo-Blanc, A., Jolivet, L. & Rossetti, F., 2004. Lateral slab deformation and the origin of the western Mediterranean arcs, *Tectonics,* **23**(1), doi:10.1029/2002TC001488.

Faccenna, C. *et al.*, 2014. Mantle dynamics in the Mediterranean, *Rev. Geophys.,* **52**(3), 283–332.

Fernàndez, M., Marzán, I. & Torne, M., 2004. Lithospheric transition from the Variscan Iberian massif to the Jurassic oceanic crust of the central Atlantic, *Tectonophysics,* **386**(1–2), 97–115.

Flecha, I. *et al.*, 2009. Seismic imaging and modelling of the lithosphere of SW Iberia, *Tectonophysics,* **472**(1), 148–157.

Fullea, J., Fernàndez, M., Afonso, J., Vergés, J. & Zeyen, H., 2010. The structure and evolution of the lithosphere–asthenosphere boundary beneath the atlantic–mediterranean transition region, *Lithos,* **120**(1–2), 74–95.

García-Mayordomo, J. *et al.*, 2012. The quaternary active faults database of Iberia (qafi v. 2.0), *J. Iberian Geol.,* **38**(1), 285–302.

Gaudot, I., 2016, Analysis of seismic ambient wavefield cross-correlations - application to the tomography of western France. *Theses,* Université de Nantes.

Geissler, W.H. *et al.*, 2010. Focal mechanisms for sub-crustal earthquakes in the Gulf of Cadiz from a dense obs deployment, *Geophys. Res. Lett.,* **37**(18), L18309.

GEOFON Data Centre, 1993. GEOFON Seismic Network, Deutsches GeoForschungsZentrum GFZ, doi:10.14470/TR560404.

Gil, A., Gallart, J., Diaz, J., Carbonell, R., Torne, M., Levander, A. & Harnafi, M., 2014. Crustal structure beneath the Rif Cordillera, North Morocco, from the RIFSis wide-angle reflection seismic experiment, *Geochem. Geophys. Geosyst.,* **15**(12), 4712–4733.

Green, P.J., 1995. Reversible jump Markov chain Monte Carlo computation and Bayesian model determination, *Biometrika,* **82**(4), 711–732.

Grevemeyer, I., Gràcia, E., Villaseñor, A., Leuchters, W. & Watts, A.B., 2015. Seismicity and active tectonics in the Alboran Sea, western Mediterranean: constraints from an offshore-onshore seismological network and swath bathymetry data, *J. geophys. Res.,* **120**(12), 8348–8365.

Grevemeyer, I., Lange, D., Villinger, H., Custódio, S. & Matias, L., 2017. Seismotectonics of the horseshoe abyssal plain and Gorringe bank, Eastern Atlantic Ocean - Constraints from ocean-bottom seismometer data, *J. geophys. Res.,* **122**(1), 63–78.

Grevemeyer, I., Matias, L. & Silva, S., 2016. Mantle earthquakes beneath the south Iberia continental margin and Gulf of Cadiz–constraints from an onshore-offshore seismological network, *J. Geodyn.,* **99 ,** 39–50.

Grünthal, G., Wahlström, R. & Stromeyer, D., 2013. The share european earthquake catalogue (SHEEC) for the time period 1900–2006 and its comparison to the European-Mediterranean earthquake catalogue (EMEC), *J. Seismol.,* **17**(4), 1339–1344.

Gutscher, M.-A., Malod, J., Rehault, J.-P., Contrucci, I., Klingelhoefer, F., Mendes-Victor, L. & Spakman, W., 2002. Evidence for active subduction beneath Gibraltar, *Geology,* **30**(12), 1071–1074.

Gutscher, M.-A. *et al.*, 2012. The gibraltar subduction: a decade of new geophysical data, *Tectonophysics,* **574–575**(0), 72–91.

Hingee, M., Tkalčić, H., Fichtner, A. & Sambridge, M., 2011. Seismic moment tensor inversion using a 3-D structural model: applications for the Australian region, *Geophys. J. Int.,* **184**(2), 949–964.

Hosseini, K., Matthews, K.J., Sigloch, K., Shephard, G.E., Domeier, M. & Tsekhmistrenko, M., 2018. Submachine: web-based tools for exploring seismic tomography and other models of earth's deep interior, *Geochem. Geophys. Geosyst.,* **19**(5), 1464–1483.

Husen, S., Kissling, E., Deichmann, N., Wiemer, S., Giardini, D. & Baer, M., 2003. Probabilistic earthquake location in complex three-dimensional velocity models: application to Switzerland, *J. geophys. Res.,* **108,** 2077.

Institut Cartogràfic I Geològic De Catalunya, 1984. Catalan Seismic Network, International Federation of Digital Seismograph Networks, doi:10.7914/SN/CA.

Institute Earth Sciences "Jaume Almera" CSIC (ICTJA Spain), 2007. IberArray, International Federation of Digital Seismograph Networks, 10.7914/SN/IB.

Instituto Dom Luiz (IDL)-Faculdade De Ciências Da Universidade De Lisboa, 2003. University of Lisbon Seismic Network, International Federation of Digital Seismograph Networks, 10.7914/SN/LX.

Instituto Geografico Nacional, Spain, 1999. Spanish Digital Seismic Network, International Federation of Digital Seismograph Networks, doi:10.7914/SN/ES.

Instituto Português do Mar e da Atmosfera, I.P., 2006. Portuguese National Seismic Network, International Federation of Digital Seismograph Networks, doi:10.7914/SN/PM.

Kennett, B.L.N., Engdahl, E.R. & Buland, R., 1995. Constraints on seismic velocities in the earth from traveltimes, *Geophys. J. Int.,* **122**(1), 108–124.

Lbadaoui, A. *et al.*, 2012. Body waves tomography from OBS-recorded earthquakes in the Gulf of Cadiz, *Int. Rev. Phys.,* **6,** 232–240.

Levander, A. & Humphreys, G., 2009. Program to Investigate Convective Alboran Sea System Overturn, International Federation of Digital Seismograph Networks, doi:10.7914/SN/XB_2009.

Lienert, B.R., Berg, E. & Frazer, L.N., 1986. Hypocenter: an earthquake location method using centered, scaled, and adaptively damped least squares, *Bull. seism. Soc. Am.,* **76**(3), 771–783.

Lomax, A., Virieux, J., Volant, P. & Berge-Thierry, C., 2000. Probabilistic earthquake location in 3D and layered models, in *Advances in Seismic Event Location, Vol. 18 of Modern Approaches in Geophysics,* pp. 101–134, eds Thurber, C. & Rabinowitz, N., Springer Netherlands.

Lozano, L., Cantavella Nadal, J.V. & Barco, J., 2020. A new 3-D P-wave velocity model for the Gulf of Cadiz and adjacent areas derived from controlled-source seismic data: application to nonlinear probabilistic relocation of moderate earthquakes, *Geophys. J. Int.,* **221**(1), 1–19.

Lynnes, C.S. & Ruff, L.J., 1985. Source process and tectonic implications of the great 1975 north atlantic earthquake, *Geophys. J. Int.,* **82**(3), 497–510.

Macquet, M., Paul, A., Pedersen, H.A., Villaseñor, A., Chevrot, S., Sylvander, M. & Wolyniec, D., Pyrope Working Group, 2014. Ambient noise tomography of the Pyrenees and the surrounding regions: inversion for a 3-D Vs model in the presence of a very heterogeneous crust, *Geophys. J. Int.,* **199,** 402–415.

Mancilla, F.D.L. & Diaz, J., 2015. High resolution Moho topography map beneath Iberia and Northern Morocco from receiver function analysis, *Tectonophysics,* **663,** 203–211.

Martínez-Loriente, S., Sallarès, V., Gràcia, E., Bartolome, R., Dañobeitia, J.J. & Zitellini, N., 2014. Seismic and gravity constraints on the nature of the basement in the Africa-Eurasia plate boundary: new insights for the geodynamic evolution of the SW Iberian margin, *J. geophys. Res.,* **119**(1), 127–149.

Matos, C., Custódio, S., Batló, J., Zahradník, J., Arroucau, P., Silveira, G. & Heimann, S., 2018. An active seismic zone in intraplate west Iberia inferred from high-resolution geophysical data, *J. geophys. Res.,* **123**(4), 2885–2907.

MedNet Project Partner Institutions, 1988. Mediterranean Very Broadband Seismographic Network (MedNet), Istituto Nazionale di Geofisica e Vulcanologia (INGV), doi:10.13127/SD/FBBBTDTD6Q.

Molinari, I. & Morelli, A., 2011. EPcrust: a reference crustal model for the European Plate, *Geophys. J. Int.,* **185,** 352–364.

Monna, S., Cimini, G.B., Montuori, C., Matias, L., Geissler, W.H. & Favali, P., 2013. New insights from seismic tomography on the complex geodynamic evolution of two adjacent domains: Gulf of Cadiz and Alboran Sea, *J. geophys. Res.,* **118,** 1587–1601.

Omira, R., Neres, M. & Batista, L., 2019. The Gloria transform fault—NE Atlantic: seismogenic and tsunamigenic potential, in *Transform Plate Boundaries and Fracture Zones,* pp. 157–167, Elsevier.

Palomeras, I., Thurner, S., Levander, A., Liu, K., Villasenor, A., Carbonell, R. & Harnafi, M., 2014. Finite-frequency Rayleigh wave tomography of the western Mediterranean: mapping its lithospheric structure, *Geochem. Geophys. Geosyst.,* **15**(1), 140–160.

Palomeras, I., Villaseñor, A., Thurner, S., Levander, A., Gallart, J. & Harnafi, M., 2017. Lithospheric structure of Iberia and Morocco using finite-frequency Rayleigh wave tomography from earthquakes and seismic ambient noise, *Geochem. Geophys. Geosyst.,* **18,** 1824–1840.

Pasyanos, M.E., Masters, T.G., Laske, G. & Ma, Z., 2014. Litho1.0: an updated crust and lithospheric model of the earth, *J. geophys. Res.,* **119**(3), 2153–2173.

Pedreira, D. *et al.*, 2015. Geophysical-petrological modeling of the lithosphere beneath the Cantabrian mountains and the North-Iberian margin: geodynamic implications, *Lithos,* **230,** 46–68.

Pinheiro, L., Wilson, R., Pena dos Reis, R., Whitmarsh, R. & Ribeiro, A., 1996. The western Iberia margin: a geophysical and geological overview, in *Proceedings of the Ocean Drilling Program Scientific Results,* pp. 3–26, National Science Foundation.

Pulgar, J., Gallart, J., Fernndez-Viejo, G., Prez-Estan, A. & lvarez Marrn, J., 1996. Seismic image of the cantabrian mountains in the western extension of the pyrenees from integrated escin reflection and refraction data, *Tectonophysics,* **264**(1), 1–19.

Rawlinson, N., Pilia, S., Young, M., Salmon, M. & Yang, Y., 2016. Crust and upper mantle structure beneath southeast Australia from ambient noise and teleseismic tomography, *Tectonophysics,* **689,** 143–156.

Rosenbaum, G., Lister, G.S. & Duboz, C., 2002. Relative motions of Africa, Iberia and Europe during alpine Orogeny, *Tectonophysics,* **359**(1–2), 117–129.

Royden, L.H., 1993. The tectonic expression slab pull at continental convergent boundaries, *Tectonics,* **12**(2), 303–325.

Salah, M.K., 2014. Upper crustal structure beneath southwest Iberia north of the convergent boundary between the Eurasian and African plates, *Geoscience Frontiers,* **5**(6), 845–854.

Salah, M.K., Chang, S.J. & Fonseca, J.F.B.D., 2011. Crustal structure beneath the lower Tagus valley, southwestern Iberia using joint analysis of teleseismic receiver functions and surface-wave dispersion, *Geophys. J. Int.,* **184**(2), 919–933.

Sallarès, V. *et al.*, 2011. Seismic evidence for the presence of Jurassic oceanic crust in the central Gulf of Cadiz (SW Iberian margin), *Earth planet. Sci. Lett.,* **311**(1–2), 112–123.

San Fernando Royal Naval Observatory (ROA), Universidad Complutense De Madrid (UCM), Helmholtz-Zentrum Potsdam Deutsches GeoForschungsZentrum (GFZ), Universidade De Evora (UEVORA Portugal), Institute Scientifique Of RABAT (ISRABAT Morocco), 1996. The Western Mediterranean BB seismic Network, Deutsches GeoForschungsZentrum GFZ, doi:10.14470/JZ581150.

Schivardi, R. & Morelli, A., 2011. EPmantle: a 3-D transversely isotropic model of the upper mantle under the European Plate, *Geophys. J. Int.,* **185**(1), 469–484.

Seillé, H. *et al.*, 2015. Crustal structure of an intraplate thrust belt: the Iberian Chain revealed by wide-angle seismic, magnetotelluric soundings and gravity data, *Tectonophysics,* **663,** 339–353.

Serpelloni, E., Faccenna, C., Spada, G., Dong, D. & Williams, S. D.P., 2013. Vertical GPS ground motion rates in the Euro-Mediterranean region: new evidence of velocity gradients at different spatial scales along the Nubia-Eurasia plate boundary, *J. geophys. Res.,* **118**(11), 6003–6024.

Shephard, G., Matthews, K., Hosseini, K. & Domeier, M., 2017. On the consistency of seismically imaged lower mantle slabs, *Sci. Rep.,* **7,** doi:10.1038/s41598-017-11039-w.

Silva, S., Terrinha, P., Matias, L., Duarte, J.C., Roque, C., Ranero, C.R., Geissler, W.H. & Zitellini, N., 2017. Micro-seismicity in the Gulf of Cadiz: is there a link between micro-seismicity, high magnitude earthquakes and active faults? *Tectonophysics,* **717,** 226–241.

Silveira, G., Stutzmann, E., Schimmel, M., Dias, N., Kiselev, S. & Dündar, S., 2016. Anisotropic tomography of Portugal (West Iberia) from ambient seismic noise , *EGU General Assembly, Geophysical Research Abstracts, Vol. 18, EGU2016-14383 , Vienna, 2016, April 17-22*.

Simancas, J.F. *et al.*, 2003. Crustal structure of the transpressional Variscan orogen of SW Iberia: SW Iberia deep seismic reflection profile (IBERSEIS), *Tectonics,* **22**(6), doi:10.1029/2002TC001479.

Smith, R.B. *et al.*, 2009. Geodynamics of the yellowstone hotspot and mantle plume: Seismic and GPS imaging, kinematics, and mantle flow, *J. Volcanol. Geotherm. Res.,* **188**(1–3), 26–56.

Snoke, J.A. & Lahr, J.C., 2001. Locating earthquakes: at what distance can the earth no longer be treated as flat? *Seismol. Res. Lett.,* **72**(5), 538–541.

Stefano, R.D., Chiarabba, C., Lucente, F. & Amato, A., 1999. Crustal and uppermost mantle structure in Italy from the inversion of p-wave arrival times: geodynamic implications, *Geophys. J. Int.,* **139**(2), 483–498.

Stucchi, M. *et al.*, 2013. The SHARE European Earthquake Catalogue (SHEEC) 1000–1899, *J. Seismol.,* **17**(2), 523–544.

Theunissen, T. *et al.*, 2017. Absolute earthquake locations using 3-D versus 1-D velocity models below a local seismic network: example from the Pyrenees, *Geophys. J. Int.,* **212**(3), 1806–1828.

USGS, Pawlewicz, M.J., Steinshouer, D.W. & Gautier, D.L., 1997a. Map showing geology, oil and gas fields, and geologic provinces of Europe including Turkey, Tech. rep., Reston, VA.

USGS, Persits, F.M., Ahlbrandt, T.S., Tuttle, M.L., Charpentier, R.R., Brownfield, M.E. & Takahashi, K.I., 1997b. Maps showing geology, oil and gas fields and geological provinces of Africa, Tech. rep., Reston, VA.

Veludo, I., Dias, N.A., Fonseca, P.E., Matias, L., Carrilho, F., Haberland, C. & Villaseñor, A., 2017. Crustal seismic structure beneath Portugal and southern Galicia (western Iberia) and the role of Variscan inheritance, *Tectonophysics,* **717,** 645–664.

Vergés, J. & Sàbat, F., 1999. Constraints on the Neogene Mediterranean kinematic evolution along a 1000 km transect from Iberia to Africa, *Geol. Soc., Lond., Spec. Publ.,* **156**(1), 63–80.

Vilanova, S.P. *et al.*, 2014. Incorporating descriptive metadata into seismic source zone models for seismic hazard assessment: a case study of the Azores–West Iberian region, *Bull. seism. Soc. Am.,* **104**(3), 1212–1229.

Villaseñor, A. *et al.*, 2015. Subduction and volcanism in the Iberia-North Africa collision zone from tomographic images of the upper mantle, *Tectonophysics,* **663,** 238–249.

Wagner, M., Husen, S., Lomax, A., Kissling, E. & Giardini, D., 2013. High-precision earthquake locations in Switzerland using regional secondary arrivals in a 3-D velocity model, *Geophys. J. Int.,* **193,** 1589–1607.

Wang, S., Niu, F. & Zhang, G., 2013. Velocity structure of the uppermost mantle beneath east Asia from Pntomography and its dynamic implications, *J. geophys. Res.,* **118**(1), 290–301.

Wessel, P. & Smith, W.H.F., 1998. New, improved version of generic mapping tools released, *EOS, Trans. Am. Geophys. Un.,* **79**(47), 579–579.

Wortel, M.J.R. & Spakman, W., 2000. Subduction and slab detachment in the Mediterranean-Carpathian region, *Science,* **290**(5498), 1910–1917.

Zeyen, H., Ayarza, P., Fernàndez, M. & Rimi, A., 2005. Lithospheric structure under the western African-European plate boundary: a transect across the atlas mountains and the Gulf of Cadiz, *Tectonics,* **24**(2), doi:10.1029/2004TC001639.

Zitellini, N., Rovere, M., Terrinha, P., Chierici, F. & Matias, L., 2004. Neogene through quaternary tectonic reactivation of SW Iberian passive margin, *Pure appl. Geophys.,* **161**(3), 565–587.

Zitellini, N. *et al.*, 2009. The quest for the Africa–Eurasia plate boundary west of the strait of Gibraltar, *Earth planet. Sci. Lett.,* **280**(1–4), 13–50.

SUPPORTING INFORMATION

Supplementary data are available at *GJI* online.

MOVIES_ESUPPLEMENT.zip

Please note: Oxford University Press is not responsible for the content or functionality of any supporting materials supplied by the authors. Any queries (other than missing material) should be directed to the corresponding author for the paper.